

Dynamic Bayesian Optimization for Improving the Performance of Cellular Networks

Author: Emanuele Mengoli

Host Institution: École Polytechnique Fédérale de Lausanne (EPFL)

EPFL Supervisors: Patrick Thiran, Anthony Bardou

École Polytechnique supervisor: Juan Antonio Cordero Fuertes

Internship Period: 15/04/2024 - 05/09/2024

Internship course code: INF690

August 28, 2024

Contents

1	Introduction	2
2	Background	3
2.1	Introduction to Bayesian Optimization	3
2.1.1	W-DBO	4
2.2	Non-Orthogonal Multiple Access (NOMA)	5
3	Problem Statement	6
4	Methodology	9
4.1	Simulator General Description	9
4.2	Mobility models	10
4.2.1	Literature analysis	10
4.2.2	Analysis of the mobility framework	11
4.3	Testbed Mobility Models	12
4.3.1	Cluster motion	13
5	Experimental results	15
5.1	Experimental Settings	15
5.2	Small scale testbed	15
5.2.1	Preliminary investigations	16
5.2.2	Discussion of Experimental Results	16

6 Current Limitations and Future Extensions	17
7 Conclusion	18
A Appendix	29
A.1 User Generation	29
A.1.1 Radial-basis distribution	29
A.2 Mobility models	29
A.2.1 Custom Probabilistic Mobility Model	29
A.2.2 hybrid-GMM Equations	31
A.3 Experimental testbed	32
A.3.1 Computational time comparison	32
A.3.2 Visual representations	32
A.3.3 Hyper-parameters of the Simulator - 12 BSs	34
A.4 Results' extended visualizations	35
A.4.1 SINRs' CDFs comparison	35
A.4.2 W-DBO's hyper-parameters comparison, aggregation by replicates	39

1 Introduction

In the evolving landscape of wireless communication, there is a growing demand for more efficient, reliable, and adaptive network solutions. As wireless networks continue to become more complex, the challenge of optimising these networks in terms of spectral efficiency and throughput has become increasingly significant. The application of machine learning has had a profound impact on the development of learning solutions that are capable of responding to the dynamic and complex nature of wireless networks [15, 28, 63]. In this context, Bayesian optimisation (BO) [19] has emerged as a potential tool to address network decision-making, particularly due to its strength in tackling black-box optimisation problems. In Section 2.1 an introduction to BO is given.

Performance evaluation of wireless networks is often conducted through objective functions that are expensive to evaluate due to the sampling frequency of throughput levels. In such settings, to maintain high sampling efficiency, a greedy strategy for the search space would result in a drastic slowdown in the decision-making process.

Consequently, BO solutions are well-suited to address this type of scenario [57, 69, 6, 7]. This paper explores the application of BO in a dynamic wireless cellular network scenario with a Non-Orthogonal Multiple Access (NOMA) resource sharing mechanism (RSM) [32]. Details on NOMA are provided in Section 2.2.

The objective of this study is to evaluate the performance of a recently introduced BO algorithm, referred to as W-DBO, i.e., Wasserstein-Dynamic Bayesian Optimization [9]. This algorithm is

specifically designed to address the challenges posed by spatio-temporal settings, making it particularly suitable for real-world wireless cellular networks where NOMA is employed as RSM. This setting inherently incorporates user mobility.

The rest of this paper is organized as follows: Section 2 highlights technical details over BO and NOMA. Section 3 provides the problem statement. Section 4 discusses the experimental tested methodology, along with a comparative study of the state of the art of motion models. In Section 5, we present our experimental results. Finally, Section 6 and Section 7 conclude the paper with a discussion of the implications of our findings and potential avenues for future research. Additional material is provided in Appendix A.

2 Background

2.1 Introduction to Bayesian Optimization

BO is a powerful probabilistic model-based method designed to optimize expensive, noisy, and complex objective functions, particularly when the underlying function is unknown and costly to evaluate.

In BO, a Gaussian Process (GP) [67] is typically employed as a surrogate model for the unknown objective function. More formally, a GP can be conceived as a collection of random variables $\{Z(\mathbf{x})\}_{\mathbf{x} \in \mathcal{A}}$ over a domain \mathcal{A} , where any finite subset of these variables follows a joint multivariate Gaussian distribution. The GP is characterized by its mean function $\mu(\mathbf{x})$ and covariance function $k(\mathbf{x}, \mathbf{x}')$, defined as:

$$\mu(\mathbf{x}) = \mathbb{E}[Z(\mathbf{x})], \quad k(\mathbf{x}, \mathbf{x}') = \mathbb{E}[(Z(\mathbf{x}) - \mu(\mathbf{x}))(Z(\mathbf{x}') - \mu(\mathbf{x}'))] \quad (1)$$

BO entails the iterative update of the surrogate model as new data points are evaluated, such that the prior GP gets updated to refine a posterior distribution over the function $f(\mathbf{x})$. An example of a GP-regression to model a surrogate function is given in Figure 1. The prior GP is specified by a mean function $\mu_0(\mathbf{x})$ and a covariance function $k(\mathbf{x}, \mathbf{x}')$, where commonly $\mu_0(\mathbf{x}) = 0$ without loss of generality and $\sigma_t^2(x) = k(\mathbf{x}, \mathbf{x}')$. The prior GP provides the foundation for computing the posterior distribution over $f(\mathbf{x})$, such that $f(\mathbf{x}) \sim \mathcal{N}(\mu_t(\mathbf{x}), \sigma_t^2(\mathbf{x}))$. Consider a set of t observations, with input data points $\mathbf{X} = (\mathbf{x}_i)_{i=1}^t$, where each \mathbf{x}_i is d -dimensional, and corresponding outputs $\mathbf{z} = (z_i)_{i=1}^t$, where each z_i is a scalar. The posterior mean $\mu_t(\mathbf{x})$ and variance $\sigma_t^2(\mathbf{x})$ are computed as:

$$\mu_t(\mathbf{x}) = \mathbf{k}(\mathbf{x}, \mathbf{X})^\top \mathbf{K}^{-1} \mathbf{z}, \quad \sigma_t^2(\mathbf{x}) = \sigma_0^2(\mathbf{x}) - \mathbf{k}(\mathbf{x}, \mathbf{X})^\top \mathbf{K}^{-1} \mathbf{k}(\mathbf{x}, \mathbf{X}) \quad (2)$$

where $\mathbf{k}(\mathbf{x}, \mathbf{X}) = (k(\mathbf{x}, \mathbf{x}_i))_{i \in [1, t]}$ and $\mathbf{K} = (k(\mathbf{x}_i, \mathbf{x}_j))_{i, j \in [1, t]}$.

In BO, the trade-off between exploration and exploitation is managed by choosing an acquisition function, which determines the next point to evaluate. Common acquisition functions include

Expected Improvement (EI) [48], Probability of Improvement (PI) [29], and Upper Confidence Bound (UCB) [1]. At each iteration, the BO algorithm selects a point \mathbf{x}_t that maximizes an acquisition function $\varphi_t(\mathbf{x})$, i.e. $\mathbf{x}_t = \arg \max_{\mathbf{x} \in \mathcal{A}} \varphi_t(\mathbf{x})$. The GP-UCB acquisition function [61], which is one of the most widely used due to its low computational complexity, is defined as:

$$\varphi_t(\mathbf{x}) = \mu_t(\mathbf{x}) + \beta_t^{1/2} \sigma_t(\mathbf{x}) \quad (3)$$

where $\mu_t(\mathbf{x})$ represents the best current estimate of $f(\mathbf{x})$ (exploitation term), and $\sigma_t(\mathbf{x})$ represents the uncertainty in the prediction (exploration term). The parameter $\beta_t^{1/2}$ controls the balance between these two factors, ensuring the algorithm achieves high-probability no-regret performance. Recent research in this field has sought to address the limitations of BO in high-dimensional spaces [8, 6, 46, 60] and space-time domain [9].

2.1.1 W-DBO

W-DBO is a recently developed BO algorithm specifically designed to handle complex spatio-temporal dynamics. In such settings the target function $f : \mathcal{S} \times \mathcal{T} \rightarrow \mathbb{R}$ is time-dependent, as well as spatial-dependent, and computationally expensive to evaluate. The spatial domain is represented by $\mathcal{S} \subseteq \mathbb{R}^d$ and $\mathcal{T} \subseteq \mathbb{R}$ denotes the temporal domain. A comprehensive technical presentation of the W-DBO algorithm can be found in [9].

In this section, we aim to highlight the main components of the W-DBO functionality to facilitate a better understanding of the remainder of this work. Consider a spatio-temporal dependent function, where $f \sim \mathcal{GP}(0, k((\mathbf{x}, t), (\mathbf{x}', t')))$, with mean 0 w.l.o.g.. To manage spatio-temporal variability, W-DBO employs a decomposition of the covariance function k into two positive correlation functions, k_S and k_T , that account for space and time, respectively. Specifically, the covariance function $k : \mathcal{S} \times \mathcal{T} \times \mathcal{S} \times \mathcal{T} \rightarrow \mathbb{R}_+$ is defined as:

$$k((\mathbf{x}, t), (\mathbf{x}', t')) = \lambda k_S(\|\mathbf{x} - \mathbf{x}'\|_2, l_S) k_T(|t - t'|, l_T), \quad (4)$$

where $\lambda > 0$ is a scaling factor, $k_S : \mathbb{R}_+ \rightarrow [0, 1]$ and $k_T : \mathbb{R}_+ \rightarrow [0, 1]$. The lengthscale parameters $l_S > 0$ and $l_T > 0$ account for space and time, respectively. The parameter λ modulates the overall magnitude of the covariance function k , while l_S and l_T control the spatial and temporal correlation lengths of the GP.

W-DBO operates by employing a Maximum Likelihood Estimation (MLE) approach to infer the parameters (λ, l_S, l_T) . To effectively assess the significance of each observation, a criterion based on the Wasserstein distance is used to compute the deviation between two GPs, differing by one removed observation. Let \mathcal{D} denote the original dataset, and $\tilde{\mathcal{D}}$ denote the dataset with one observation removed. The 2-Wasserstein distance [30] is employed to determine the shift between two distributions, as shown in Equation (5), at a point (\mathbf{x}, t) , and consequently of two GPs (considering the entire domain) as shown in Equation (6).

$$W_2(\mathcal{N}_{\mathcal{D}}(\mathbf{x}, t), \mathcal{N}_{\tilde{\mathcal{D}}}(\mathbf{x}, t)) = \left((\mu_{\mathcal{D}}(\mathbf{x}, t) - \mu_{\tilde{\mathcal{D}}}(\mathbf{x}, t))^2 + (\sigma_{\mathcal{D}}(\mathbf{x}, t) - \sigma_{\tilde{\mathcal{D}}}(\mathbf{x}, t))^2 \right)^{\frac{1}{2}}. \quad (5)$$

$$W_2(\mathcal{GP}_{\mathcal{D}}, \mathcal{GP}_{\tilde{\mathcal{D}}}) = \left(\oint_S \int_{t_0}^{\infty} W_2^2(\mathcal{N}_{\mathcal{D}}(\mathbf{x}, t), \mathcal{N}_{\tilde{\mathcal{D}}}(\mathbf{x}, t)) d\mathbf{x} dt \right)^{\frac{1}{2}}. \quad (6)$$

Note that the inferred parameters (λ, l_S, l_T) directly influence the magnitude of the Wasserstein distance, as they affect the dimensional properties of the distribution. Consequently, these parameters play a crucial role in determining which observations are subject to removal.

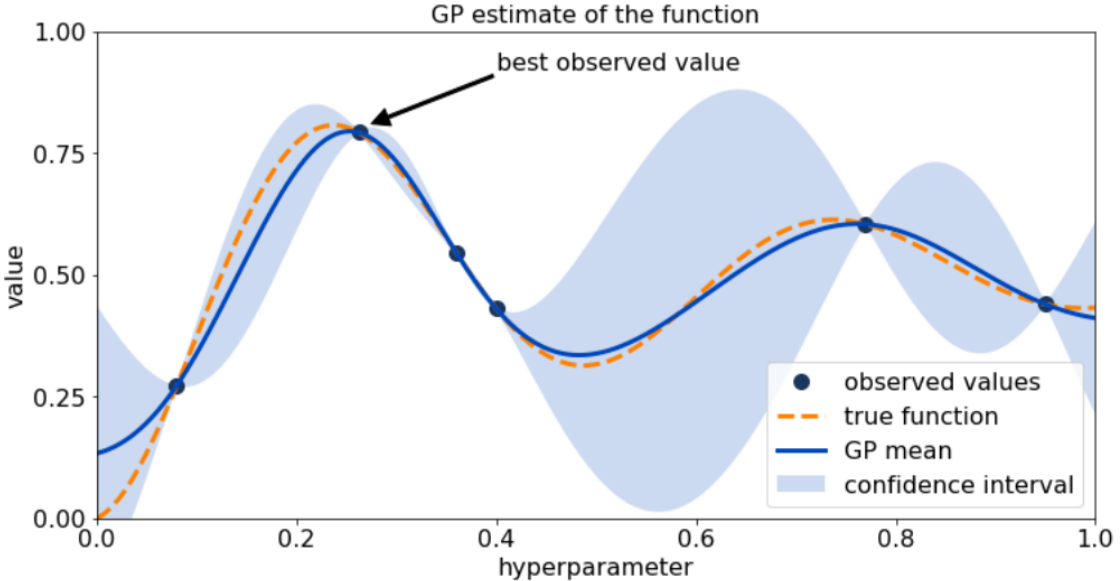


Figure 1: Example of BO procedure using GP. Image source [31].

2.2 Non-Orthogonal Multiple Access (NOMA)

The technique of superposition coding (SC), initially developed for the Gaussian broadcast channel (G-BC), is the foundation of NOMA, whereby multiple users' data streams are superimposed [58]. In a base station (BS) cell, NOMA defines two service regions associated with two distinct power levels: an inner power level and an outer power level. The outer power level is larger than the inner power level to enable efficient decoding [33, 58, 22, 12]. In contrast to Orthogonal Multiple Access (OMA) schemes such as Orthogonal Frequency Division Multiplexing (OFDMA), NOMA enables each user to utilize the entire available spectrum, as illustrated in Figure 2.2. This capability is made possible through the Successive Interference Cancellation (SIC) technique, which allows for the recovery of original signals despite the overlap in spectrum usage. Specifically, let us refer to

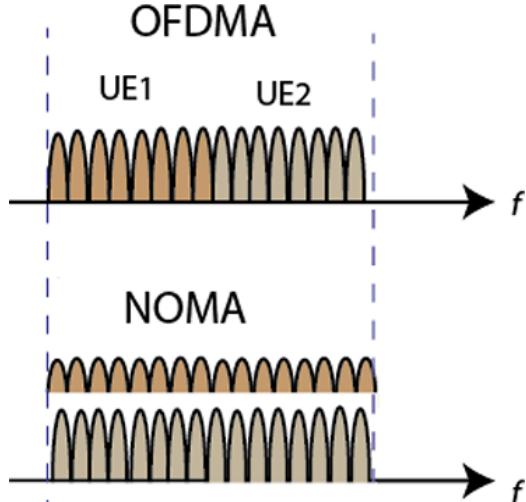


Figure 2: Spectrum sharing for two users, NOMA vs OFDMA. Image source [33].

UEs belonging to the inner region of their BS as inner UEs and symmetrically, UEs belonging to the outer region as outer UEs. Under this scheme, inner UEs decode first the signal for outer UEs and cancel their interference, whereas outer UEs decode only their own signal. The latter do not experience strong interference from inner UE signals due to the power ratio constraint, i.e. $\frac{p_i^{(\text{in})}}{p_i^{(\text{out})}} \leq 1$.

In a two-user NOMA setting, NOMA achieves the Shannon capacity limit for the Gaussian broadcast channel (G-BC), in contrast to Orthogonal Multiple Access (OMA). This is demonstrated in [22], where the capacity for a single cell with massive access is expressed.

3 Problem Statement

The framework examined in this study investigates a wireless cellular network utilizing NOMA as RSM, with users following a specified motion model. Our objective is to evaluate and compare several power allocation strategies, including the previously introduced W-DBO, to determine which strategy maximizes performance, as measured by downlink throughput. A comprehensive discussion of the motion models employed is provided in Section 4.2.

The system consists of a set of BSs $\mathcal{N} = \{1, \dots, n\}$ and a set of user equipments (UEs) $\mathcal{M} = \{1, \dots, m\}$ distributed over the area Ω . Each UE is associated with the BS that provides the highest signal-to-interference-plus-noise ratio (SINR). We assume that each BS has a minimum transmission power of P_- and a maximum transmission power of P_+ . The NOMA RSM is employed [33, 58, 22, 12]. This RSM divides each cell into two regions, thus defining two transmission power levels $\mathbf{p}_i = (p_i^{(\text{in})}, p_i^{(\text{out})})$ for each BS_i , where $i \in \mathcal{N}$. Additionally, each \mathbf{p}_i must satisfy a power constraint such that $P_- \leq \|\mathbf{p}_i\|_1 \leq P_+$. An inherent constraint for efficient decoding is that

$p_i^{(\text{in})} \leq p_i^{(\text{out})}$. These two constraints are mapped into a bijection, defined as follows:

$$\underbrace{\left(p_i^{(\text{in})}, p_i^{(\text{out})}\right)}_{\mathbf{p}_i} \rightarrow \underbrace{\left(p_i^{(\text{in})} + p_i^{(\text{out})}, \frac{p_i^{(\text{out})}}{p_i^{(\text{in})} + p_i^{(\text{out})}}\right)}_{\mathbf{x}_i} \quad (7)$$

Consequently, the cellular network parameters are defined by the vector $\mathbf{x} = (\mathbf{x}_1, \dots, \mathbf{x}_n) \in \mathcal{D}$, where \mathcal{D} is a rectangular parameter space:

$$\mathcal{D} = \bigtimes_{w=1}^n \mathcal{D}^{(w)} = \left([P_-, P_+] \times \left[\frac{1}{2}, 1\right]\right)^n \quad (8)$$

where \times is generalized cartesian product.

We consider a set of UEs, indexed by $j \in [1, m]$, such that for a given cellular network configuration \mathbf{x}_t , the achievable rate is denoted by $c^{(j)}(\mathbf{x}_t)$. Therefore, the performance metrics at the cellular network level are given by $\mathbf{c}(\mathbf{x}_t) = (c^{(1)}(\mathbf{x}_t), \dots, c^{(m)}(\mathbf{x}_t)) \in \mathbb{R}^m$.

The natural objective of the model is to maximize the overall downlink capacity, yielding the highest Quality of Service (QoS) for the end-users. The problem is tackled in a decentralized manner, operating under the assumption that the interference experienced by user j , associated with BS i , originates exclusively from the neighbourhood of BS i , denoted by \mathcal{N}_i .

Let $|\mathcal{N}_i|$ represent the cardinality of \mathcal{N}_i , and let $\mathcal{A} = \{\mathcal{A}^{(1)}, \dots, \mathcal{A}^{(2n)}\}$ be a partition on Ω , obtained by considering the BSs' service areas while using NOMA.

The performance of the cellular network is quantified by the objective function $F_\alpha(c_t)$, which is designed to be optimized and reflects the downlink capacity. To transform the network parameters into scalar values, we apply the concept of α -fairness [47]. This approach yields the following equation:

$$F_\alpha(c_t) = \begin{cases} \sum_{i=1}^m \log c_t^{(j)} & \text{if } \alpha = 1, \\ \sum_{j=1}^m \frac{(c_t^{(j)})^{1-\alpha}}{1-\alpha} & \text{otherwise,} \end{cases} \quad (9)$$

where $c_t^{(j)}$ denotes $c^{(j)}(\mathbf{x}_t)$.

Despite NOMA's capability for full spectrum sharing, scheduling remains essential for efficiently allocating available resources to the served users. To achieve this, we can leverage knowledge of the users' capacities. The optimal scheduling strategy for a set $\mathcal{A}^{(k)}$ of UEs is given by $\mathbf{s}^{(k)} = (s_j^{(k)})_{j \in \mathcal{A}^{(k)}}$, where:

$$s_j^{(k)} = \begin{cases} \mathbb{1}_{j=j^*} & \text{if } \alpha = 0, \\ \frac{(c_t^{(j)})^{(1-\alpha)/\alpha}}{\sum_{i \in \mathcal{A}^{(k)}} (c_t^{(i)})^{(1-\alpha)/\alpha}} & \text{otherwise,} \end{cases} \quad (10)$$

with $j^* = \arg \max_{j \in \mathcal{A}^{(k)}} c_t^{(j)}$, where $\mathbb{1}_{j=j^*}$ denotes the indicator function that identifies the index of the UE with the highest rate among those in the set $\mathcal{A}^{(k)}$ ¹.

We define the function $f_\alpha^{(i)} : \mathcal{D}^{(\mathcal{N}_i)} \rightarrow \mathcal{D}$, where $\mathcal{D}^{(\mathcal{N}_i)} = \times_{i' \in \mathcal{N}_i} \mathcal{D}^{(i')}$, as follows:

$$f_\alpha(\mathbf{x}_t) = \sum_{i=1}^n \sum_{\mathcal{A}^{(k)} \in \mathcal{A}_i} \sum_{j \in \mathcal{A}^{(k)}} F_\alpha \left(\mathbf{s}^{(k)} \odot \mathbf{c}^{(k)} \left(\mathbf{x}_t^{(\mathcal{N}_i)} \right) \right) \quad (11)$$

By slightly modifying Equation (11), an additive decomposition form can be derived, see Equation (12). This form is utilized to mitigate high dimensionality and reduce the computational complexity of the problem.

$$f_\alpha^{(i)} \left(\mathbf{x}_t^{(\mathcal{N}_i)} \right) = \sum_{i' \in \mathcal{N}_i} \sum_{\mathcal{A}^{(k)} \in \mathcal{A}_{i'}} \sum_{j \in \mathcal{A}^{(k)}} \frac{F_\alpha \left(\mathbf{s}^{(k)} \odot \mathbf{c}^{(k)} \left(\mathbf{x}_t^{(\mathcal{N}_{i'})} \right) \right)}{|\mathcal{N}_{i'}|}. \quad (12)$$

Thus, it is straightforward to show that:

$$f_\alpha(\mathbf{x}_t) = \sum_{i=1}^n f_\alpha^{(i)} \left(\mathbf{x}_t^{(\mathcal{N}_i)} \right) \quad (13)$$

Equation (13) defines the objective function to be optimised. To compute the received power levels required for the Shannon capacity, we use the log-distance path loss model. In such model, the path-loss L is determined as follows:

$$L = L_{\text{Tx}} - L_{\text{Rx}} = L_0 + 10\gamma \log_{10} \left(\frac{d}{d_0} \right) + X_g \quad (14)$$

where L_{Tx} and L_{Rx} are the transmission and reception losses, respectively. The term L_0 denotes the path loss at a reference distance d_0 , γ is the path loss exponent reflecting the environment, and X_g is a Gaussian random variable representing the shadowing effect. Detailed descriptions of these parameters are provided in Appendix A.3.3.

Thus, knowing the gain (i.e., the inverse of the path-loss in linear scale), we can define the SINR formulation using NOMA RSM. Following this setting a closed form for the SINR of two users, namely inner UE j and outer UE j' , associated with BS i , can be derived and is denoted by $\gamma_{i,j}^{(\text{in})}$ and $\gamma_{i,j'}^{(\text{out})}$, respectively:

$$\gamma_{i,j}^{(\text{in})} = \frac{g_{i,j} p_1^{(i)}}{WN + \sum_{i' \in \mathcal{N}_i \setminus \{i\}} g_{i',j} (p_1^{(i')} + p_2^{(i')})} \quad (15)$$

$$\gamma_{i,j'}^{(\text{out})} = \frac{g_{i,j'} p_2^{(i)}}{WN + g_{i,j'} p_1^{(i)} + \sum_{i' \in \mathcal{N}_i \setminus \{i\}} g_{i',j'} (p_1^{(i')} + p_2^{(i')})} \quad (16)$$

¹A full proof is provided in an ongoing publication, not yet available, i.e., Bardou A. et al., “Assessing the Performance of NOMA in a Multi-Cell Context: A General Evaluation Framework”.

Where N is the noise power density defined as dBm/Hz , W is the signal bandwidth and $g_{i,j}$ is radio link gain between BS i and UE j .

It follows that the downlink Shannon capacity for UE j is:

$$c^{(j)} = c(\gamma_{i,j}) = W_j \cdot \log_2(1 + \gamma_{i,j}). \quad (17)$$

4 Methodology

4.1 Simulator General Description

The testbed logic integrates several key components to model the behaviour and performance of cellular networks in a realistic urban environment. The set of BSs is retrieved from Parisian available city data [18], with the goal of replicating a real-world scenario and infrastructure placement. We aim to simulate the LTE infrastructure given the larger presence of LTE sites over 5G sites (734 LTE sites vs 154 5G sites [18]). In the initialization step, the simulator user has the choice to instantiate an arbitrary number of UEs in the system, placed following a uniform distribution over the grid. Alternatively, the first pool of UEs is placed following either a Poisson point process [3], Log-Gaussian Cox process [49] or a Radial-basis distribution (see Appendix A.1.1 for the details), in order to assure that a baseline population will roam continuously in the network without being removed. This, to avoid sudden changes in the volume of users would affect the optimizer's performances. Nevertheless, UEs are subjected to a birth and death (B&D) process, modelled as a standard M/M/1 queue [34]. This is a straightforward yet effective approach to modelling the arrival and living time of UEs within a network [56].

Upon the birth of a new user, its placement follows a uniform probability distribution over the grid. Within the network area, UEs' motion follows the models discussed in Section 4.3. Alternatively, the testbed supports the upload of an external file containing the real-world recorded traces of a set of UEs. The simulation will then iterate over those traces, moving the associated UEs accordingly. The UE-BS allocation policy pairs UEs with the BS that provides the highest SINR, considering only the BS's outer power for the SINR calculation. The optimization model (i.e., W-DBO, Random pick, Constant pick) is applied in two scenarios. First, it is used to determine the optimal power level within a BS's neighbourhood, where a given BS receives power level suggestions from neighbouring BSs. Neighbours are defined as BSs located within the nominal coverage area of a given BS. The second application involves partitioning the inner and outer regions of UEs for a given BS. This method seeks to identify the SNR threshold that distinguishes inner UEs from outer UEs, where inner UEs have an SNR greater than the threshold, and outer UEs have an SNR lower than the threshold. To determine this threshold, all UEs served by a BS are sorted by SNR in descending order. The combination of inner and outer users that maximizes the objective function value (13) defines the threshold. Our approach assumes that intra-cell assignment occurs after users motion and subsequently network performance data are collected. Border BSs are filtered out to avoid border effects.

4.2 Mobility models

4.2.1 Literature analysis

To replicate a real-world scenario, UEs are subject to movement across the network, Ω . A comprehensive overview of mobility models for wireless networks is provided in [11, 5, 26]. Camp et al. [11] analyzed both group and entity mobility models for ad-hoc networks, in order to stress-test novel protocol robustness. A few proposed models, later discussed in Section 4.2.2, are also used in the literature of cellular networks to approximate UEs' trajectories [20, 36, 10, 37, 25]. Bai et al. [5] extended [11] by focusing on group mobility models. A Java-based open software implementation, which builds on [11], is presented in [50]. Similarly, [17] proposed a visual tool to observe taxi traffic mobility and trajectories based on the city of New York.

González et al. [21] provided a statistical measure of human routine dynamics, highlighting the intrinsic high degree of temporal and spatial regularity in human trajectories, with a significant probability of returning to a few highly frequented locations. The work suggests that pure random trajectories computed through Lévy flights and random walk models result in a high degree of inaccuracy.

Yan et al. [68] proposed a universal mobility model that primarily exploits information on population distribution. Their idea extends the radiation model [59], overcoming the latter's limitations in city-scale dynamics. In essence, the authors' contribution of [68] lies in the proposal of computing the probability map of potential destinations through the population density of a given area. The model is based on the assumption that the attractiveness of the destination is given by the opportunities of the destination itself, inversely weighted by the population present between the destination and the origin. However, this assumption ceases to be valid when one considers the structure of European cities, whose architecture resembles concentric circles that gradually expand. In these scenarios, the population density tends to decay following a radial distribution, centred on the historical sector of the city, e.g. the area surrounding the cathedral or major business districts (e.g. La Défense, Paris). Such areas are likely to act as destinations or transit points for frequent routine traffic flows, despite the population density peaks that may lie within the routes. The Roman heritage of the "Cardus-Decumanus" for urban planning remains pertinent, as historic centres are typically the central node of commuter lines connecting the city's antipodes. Furthermore, in general, museums and historic buildings are located within the historic centre, representing the largest area of interest for tourist activity, hence a significant destination of ulterior periodic urban flow.

For a more realistic approach, trajectories have been estimated and studied through several means: road Access Points (APs) [64], mobile phone signalling data [23], Call Detail Records (CDR) [4], and historical data from CDR, GPS, and WiFi traces [27].

Human mobility interpretation represents another stream of research, as highlighted by Loder et al., [39]. The authors proposed an interpretation framework for mobility behaviours to identify flow-critical points that could lead to congestion.

Several works concern the reducibility of high-dimensional traffic datasets, such as [62], which leverages a Bayesian factorization framework to retrieve the inner spatial-temporal structure of a city in lower dimensions.

Uppoor et al., [65] made a step forward in vehicle mobility, following the lead of [35], by building a large-scale dataset descriptive of the Köln urban scenario.

Remarks: Most of the works described above leverage historical data from different sources and cities aggregated with different time windows. This poses issues in terms of generalizability since traffic trajectories are inherently shaped by the urban morphology and structure, as well as city dimensions and historical heritage of the considered urban scenario. European urban mobility scenarios are significantly different from their Asian or American counterparts due to the lower presence of skyscrapers and the medieval heritage of wall-protected concentric circles that have expanded radially over time. This is the case for cities like Paris, for example.

The Parisian mobility landscape has been modeled and analyzed in [4]. The proposed approach uses traffic data from CDR to model human behaviour. Origin-Destination flows are estimated by employing the likelihood of the means of transportation, obtained from the given training set of trajectories. The full area of interest is divided into Voronoi sectors.

Finally, a few Python packages have been developed to include a wide range of random distributions for shaping mobility models: [45, 54]. The former allows building trajectories by knowing points of interest within a given area, and the latter allows generating paths by choosing a specific distribution. Lastly, the Python package proposed in [53] implements the majority of the models presented in [11].

4.2.2 Analysis of the mobility framework

Our case scenario encompasses complex network dynamics, characterized by clusters of UEs populating the environment and subjected to spatial translation over time. Hence, a realistic scenario should consider the directional constraints posed by the territory morphology and the transport infrastructure, accompanied by its endemic mobility limits (i.e., velocity, direction, density...). The high degree of complexity would require access to the city's available data, allowing the understanding of the Origin/Destination (O/D) flows, the population distribution, the traffic magnitude, and its distribution over time. Accessing the data would also allow trajectory interpretability, highlighting the main points of interest within the city and the purpose of travel, enabling estimates of UEs' trajectories and flow magnitude. With this consideration and introducing the assumption of a rational user, we can ease the probabilistic transition model as proposed in Appendix A.2.1.

As emerged from the available literature, mobility models can be divided into two main categories: trajectory-based and distribution-based [38]. The former approach results in a more realistic and scenario-dependent modelisation, thereby enabling more precise simulation dynamics. The latter facilitates computational efficiency at the cost of increased approximation [38, 5]. This suggests that a first baseline for assessing the W-DBO algorithm can be built through a simple random mobility

model that approximates user trajectories by sampling motion key parameters through fixed distributions. Consequently, the W-DBO algorithm can be stress-tested against multiple scenarios of ascending complexity, i.e. different motion models, as proposed in Section 4.3. It's noteworthy that within the trace-based family, the Random Waypoint (RWP) model is a commonly used mobility model. This is a trajectory-based approach where nodes travel towards destination points (i.e., waypoints) sampled uniformly in the simulation area [20, 36, 10, 37, 25, 38]. Upon reaching the target, UEs are subjected to a pause time, randomly sampled. The degree of randomness inherent to this model lies in the waypoint selection, pausing time, and velocity. Consequently, it is possible to select distributions or models that aim to make these parameters as realistic as possible. In this regard, the work [10] suggests that the average speed of cars and pedestrians, within an urban scenario, can be assumed to be Rayleigh/Rice distributed, along with the assumption that road lengths follow the same type of distribution. Therefore, combining the two would ease the problem of choosing the appropriate velocity distribution in RWP. An alternative approach is to utilise the Gauss–Markov Mobility Model (GMM) to model the unknown motion parameters. The GMM maintains a memory of the spatio-temporal characteristics of a trajectory, including direction and velocity [38, 11]. Thanks to the Markovian property, velocity and direction are subjected to smooth changes over time. The degree of randomness inherent to this model can be adjusted by injecting fixed destinations (i.e. waypoints), thus constraining the trajectories. This permits the relaxation of the hypothesis of fixing motion parameters *a priori*, or in general, the immutability of those parameters during a transition. This modelisation introduces a certain degree of randomness that helps to simulate a more realistic behaviour of UEs during translations. The term *hybrid-GMM* is used herein to identify the mixture of RWP and GMM. In practical terms, the hybrid-GMM is applied to the cluster centroid, resulting in the displacement of the associated UEs. The model formulation is proposed in Appendix A.2.2.

4.3 Testbed Mobility Models

This section introduces a variety of user-based and cluster-based mobility models encompassed in our simulator. The objective is to allow the simulator end-user to stress-test the optimization models under different UE motion conditions.

The user-based mobility models investigated include the Random Walk model, where both the velocity (\vec{v}) and direction (θ) are sampled from a uniform distribution, resulting in an unstructured and erratic movement pattern. In contrast, the Biased Random Walk model introduces an additional layer of direction bias, by incorporating bias direction (θ') and bias strength (β), which are also uniformly sampled. This model allows for a more directed movement, reflecting scenarios where there might be a tendency or preference in the movement direction. The Lévy flight model [42], which is known for its heavy-tailed step length distributions, is characterized by a parameter α within the range $0.1 \leq \alpha < 2$. Lévy flights are known for producing occasional long jumps, contrasting with the more localized movements of a random walk. Its variant, the Truncated Lévy

flight [43, 44, 14], adopts a finite variance on the step lengths, ensuring that the movement remains within a bounded region, thus avoiding the extremely long jumps seen in standard Lévy flights. Note that the Brownian motion, which can be seen as a special case of the Lévy Flight, specifically by setting α to 2, is included in the motion models set. Lastly, the RPW model [53], known for its widespread use in mobility modelling, is considered. Commonly used in simulations, in this model movement occurs towards randomly selected destinations within a bounded area, followed by pauses, effectively capturing the start-stop nature of human travel, mimicking real-world human movement patterns.

4.3.1 Cluster motion

In addition to user-based models, we explore cluster-based mobility models, focusing specifically on the hybrid-GMM model. This model simulates scenarios where UEs tend to travel together (e.g., on a common means of transport) towards specific hotspots or points of interest. A set of points within the cellular network is selected as traffic flow destinations, based on the spatial density of BSs. The DBSCAN algorithm [16] is used to identify major areas of concentration, as shown in Figures 3. The centroids of these clusters are then computed to determine the destination points. The rationale for this approach lies in the assumption that the number of BSs per square meter is proportional to the traffic flow experienced in a given geographical area, thereby allowing the identification of major urban concentration points.

Upon spawning, UEs are clustered using the K-means algorithm [41] to determine the centroid coordinates on which the translation will be applied. The cluster can be thought of as a means of transport with an average velocity (obtained through Monte Carlo (MC) sampling from a uniform distribution, defined by the minimum and maximum velocities associated with the UEs) and a direction towards a destination. The model equations are provided in Appendix A.2.2. To ensure realism, in accordance with the RPW model, at each transition step with a certain probability the cluster will pause at its current location. Clusters that reach a ψ -sufficiently close position - where the ℓ_2 -norm between the current position and the destination is less than or equal to ψ - select a new destination from the available set, following a uniform distribution. After each centroid is moved, the associated UEs are uniformly distributed around it, adding an additional marginal degree of randomness to the model.

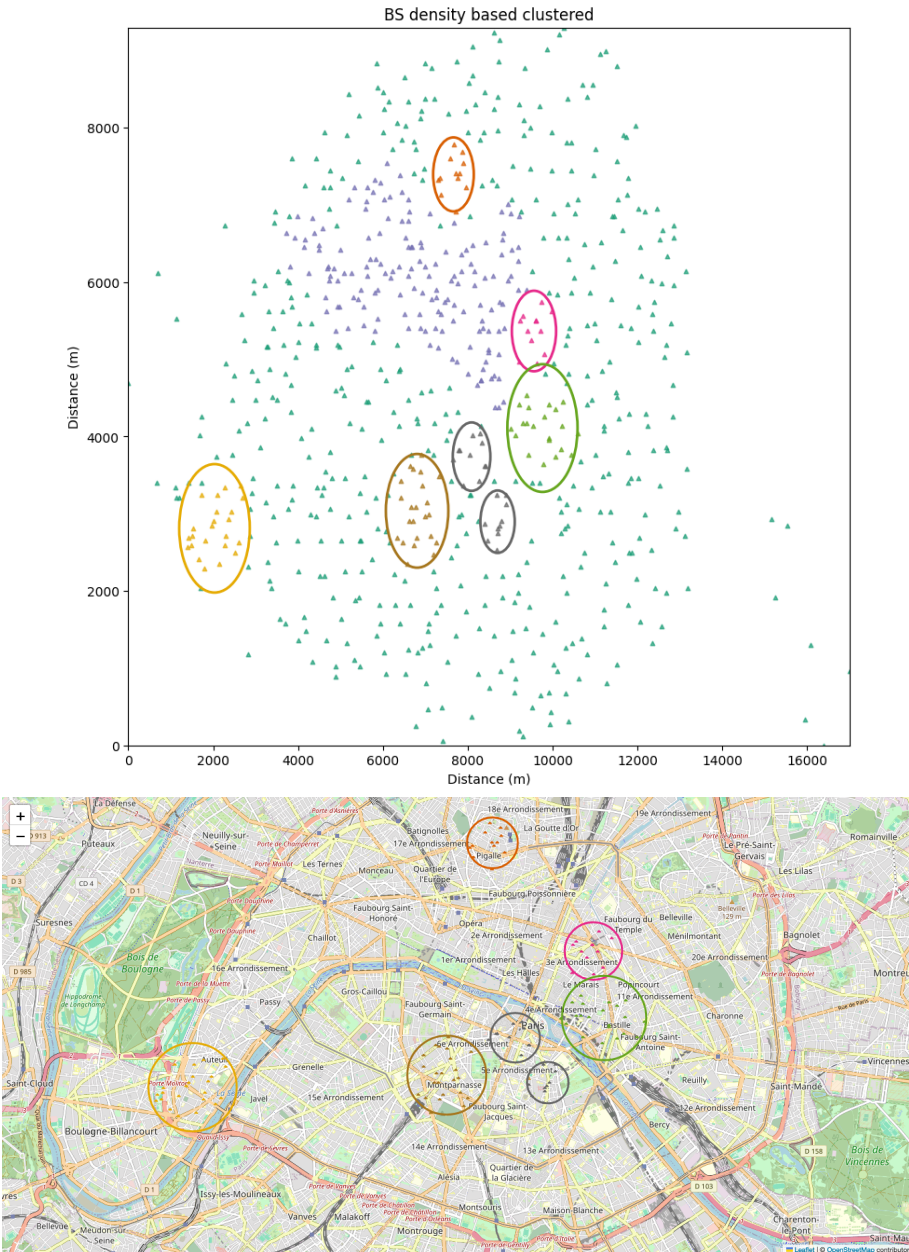


Figure 3: Both images show BSs clustered via the DBSCAN algorithm. The latter provides a geo-referenced viewpoint, build using [55, 52] tools.

5 Experimental results

5.1 Experimental Settings

For the purpose of our testbed, we benchmark the performance of W-DBO against a Random Pick model and a Constant power pick model. In the former, at each optimization round t the vector $\mathbf{x}_{\text{rndm}}^{(t)}$ is uniformly sampled from the parameter space \mathcal{D} , whereas in the latter $\mathbf{x}_{\text{const}} \in \mathcal{D}$ is sampled just once, during the first round. On the other hand, W-DBO instances collaborate to each define a different power level suggestion for a common neighborhood, i.e., $\mathbf{x}_{\text{wdbo},i}^{(t)} \in \mathcal{D}^{(i)}$, $\forall i \in \mathcal{N}$. From these suggestions, the median is calculated to determine the power levels for each BS, i.e., $\mathbf{p}_i = \text{MEDIAN}_{i' \in \mathcal{N}_i}(\mathbf{p}_{i'})$, $\forall i \in \mathcal{N}$, where each \mathbf{p}_i can be retrieved through the bijection described in Equation (7). The testbed’s episode frequency is set to 1s , corresponding to an LTE radio frame duration of $T_s = 10\text{ ms}$ [13, 66], which results in the transmission of 100 packets per episode. The motion frequency, and subsequently the optimization procedure, is set to 2s . This configuration ensures that the simulator operates with sufficient temporal granularity for capturing transient phenomena in the network. We compared the performance of the three power-picking strategies against three motion models: Biased Random Walk, RPW model and hybrid-GMM. The simulator hyper-parameters are outlined in Appendix A.3.3. The baseline of our experimental setting is a small-scale scenario with 12 BSs in an area of 2.64 km^2 , with a BS areal density of 4.55. This density imposes a minimal coverage area per BS of approximately 470m. An optimizer instance is associated to each BS. The parameters for the UE’s B&D process are chosen to prevent significant fluctuations in the number of users across rounds. The alpha fairness parameter is set to 1. The objective function is divided by the population size to avoid bias introduced by the B&D process. A visualization tool has been developed that allows users to view either a snapshot of the simulation, with the option to select the number of traces to be plotted, or a GIF-based version that shows the simulation evolving over time, frame by frame. Details of this tool are provided in Appendix A.3.2, with a link to access GIF-based visualizations.

5.2 Small scale testbed

For our experiments, we use a MacBook Pro with a 2.9 GHz Dual-Core Intel Core i5 processor and 16 GB of 2133 MHz LPDDR3 memory. The computational times for each experiment are presented in Table 1. Given the machine’s limited computational resources, we parallelize the dataset update and cleaning for W-DBOs using two concurrent threads.

All motion models, except for the RPW model, were directly implemented in the simulator. To ensure consistency across replicates, a common seed is used, allowing each replicate of a given motion model to follow the same trajectory. For the RPW model, a different approach is employed using the Python library [53]. We perform an initial simulation to record the UE traces and then inject these traces into the simulator as a benchmark for subsequent simulations.

5.2.1 Preliminary investigations

Preliminary investigations revealed that increasing the number of simulation rounds dramatically affects the results of the constant picking strategy. This behaviour contradicts the property that, as the number of simulation replicates approaches infinity, the mean of the constant picking strategy should match the mean of the random picking strategy. Although the constant picking strategy involves a single random pick at the beginning of the simulation, which then fixes the power configuration for the entire simulation period, the random picking strategy performs a new sampling at each round. As the number of replicates increases, the temporal mean obtained through the random picking strategy tends toward the statistical mean, as expected in any ergodic process with respect to the mean. Therefore, we expect that the mean of the constant picking strategy will tend to match the mean of the random picking strategy, but with an increased standard error due to the larger variance observed.

In practice, this behaviour is not observed, as shown in Figures 5. To further support this analysis, we studied a mixed strategy in which half of the base stations maintain a constant configuration, while the other half perform a random pick at each round. We refer to this mixture as the constant prime strategy. Please refer to Figure 6 for details, which shows the results of this strategy under the Biased Random Walk motion model.

The reason for this behaviour is due to the border effect filtering. As we increase the number of replicates, we may end up in a configuration where the highest user density is located on BSs outside the effective border perimeter. Fixing the power configuration *a priori*, as in the constant picking strategy, implicitly imposes a deterministic rationale on user assignment, such that BS's user density tends to remain constant across rounds. This means that UEs assigned to BSs outside this region are not considered in the performance measurements, leading to a misleading increase in the objective function due to the lower population accounted for in the performance measurement. Note that in the random pick configuration, this phenomenon can also be observed when sudden spikes occur in the objective function. However, in the long run, this effect is mitigated due to continuous oscillations in power levels, resulting in a different network configuration at each round. Lastly, note that W-DBO operates to maximize the objective function with a ratio that implies cooperation between neighbouring BSs. This logic prevents occurrences of drastic imbalances in UE-BS allocation, thereby avoiding scenarios where out-border BSs have the highest UE density. Having observed this phenomenon, we can exclude simulations in which the fixed configuration leads to this polarized scenario, which would bias our results.

Therefore the cleaned results showed that W-DBO outperformed both the Random Pick and Constant Pick models across all three mobility models, as we can observe in Figure 4.

5.2.2 Discussion of Experimental Results

The behaviour of W-DBO varies significantly depending on the motion model used, as illustrated by the shape of the objective function. This variation is noticeable especially when comparing the

hybrid-GMM model (Figures 4e, 4f) to the Biased Random Walk (Figures 4a, 4b) and RPW models (Figures 4c, 4d). Specifically, the RPW and Biased Random Walk models exhibit relatively stable behaviour, whereas the hybrid-GMM model shows more variable patterns.

This disparity can be attributed to the unique characteristics of motion dynamics, where considering moving clusters implicitly defines gaps within the network. This mechanically creates situations of UE density depression in certain areas of the network, while simultaneously generating peaks of UE presence in other areas, depending on the size of the cluster (in terms of associated users). Indeed, the constant configuration serves as evidence of this dynamic. When users move independently but have destinations or directions uniformly sampled across the network, as seen in models like the Biased Random Walk and RPW, the objective function of the constant configuration exhibits stable behaviour. This suggests that such models are not sufficiently complex to induce substantial dynamics within the network. In contrast, the hybrid-GMM model induces greater dynamism.

Similarly, this evolution is illustrated by changes in the hyper-parameters within the W-DBO throughout the learning phase, as shown in Figures 7. A set of visualizations at W-DBO instances granularity, aggregating 7 replicates, is provided in the Appendix, in Figures 11, 12, 13. Note that time is normalized for the proper functioning of W-DBO. Specifically, the dataset size for the hybrid-GMM model exhibits a more oscillatory trend compared to the other two models, which show smoother trends, as seen in Figures 7a, 11. It is noteworthy that the Biased Random Walk model is the only one that shows an increase after time 0.6. This is also evidenced by the temporal lengthscale curve in Figures 7b, 12.

The temporal lengthscale, which governs the selection of observations to be excluded from the W-DBO dataset, plays a crucial role in the inference capabilities of W-DBO. This parameter essentially defines the correlation between consecutive observations and serves as the scale parameter for W-DBO's temporal kernel. Observations below the threshold derived from the ratio of optimization frequency to total simulation time - approximately 1 in our case - are classified as uncorrelated, leading W-DBO to exclude them.

Indeed, the decrease in dataset size for the hybrid-GMM and RPW models can be attributed to the drop in the temporal lengthscale below the reference threshold for these two models. In contrast, for the Biased Random Walk model, the mean curve generally remains above the threshold.

Lastly, note that the parameter *n_initial_observations* is set to 15 (see Table A.3.3), meaning that during the first 15 iterations, W-DBO instances accumulate data and perform a random search to determine power levels. During this initial phase, the spatial and temporal lengthscales are not inferred. After the 15th iteration, data cleaning and inference processes commence.

6 Current Limitations and Future Extensions

The experimental results demonstrate that the objective function remains relatively constant, indicating that the small-scale settings with simple motion dynamics do not provide sufficient variability to justify the use W-DBO. Consequently, future extensions will focus on larger-scale simulations,

specifically involving more than 30 BSs. Increasing the network size is expected to increase the scenario’s complexity, allowing for a more thorough evaluation of W-DBO’s performance. This expansion should be accompanied by an increased complexity in the motion dynamics, potentially adopting a cluster-based approach and allowing users to change clusters over time. Leveraging correlated user mobility is crucial to influence the time variability of the objective function, as preliminary observed by adopting hybrid-GMM. Furthermore, future work will integrate real urban mobility traces [70], to achieve more realistic motion simulations.

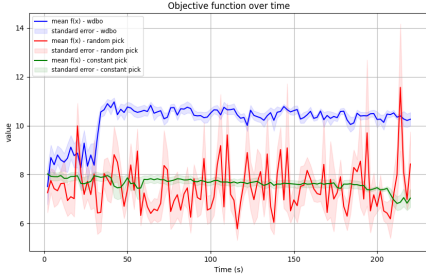
Further investigations are needed to understand the specific reason for the decaying behavior in W-DBOs’ dataset size curves for RPW and hybrid-GMM. Another potential area for extension is the duration of the simulation. In the current study, simulations were limited to 220 seconds due to computational constraints. Future research will extend the simulation period to a virtual timeline of over 30 minutes to more effectively capture and analyze real-world scenarios with greater depth. Ongoing efforts are aimed at implementing a control procedure to automatically exclude simulations in which the outer-border BSs exhibit the highest UE density. The optimal threshold value for UE density is currently under investigation.

Lastly, a W-DBO power update variant will be studied. In this setting, BSs’ power adjustments are constrained within a confidence interval centred around the previous power levels. This means that for two consecutive rounds, t and $t + 1$, the condition $\left\| \mathbf{p}_i^{(t)} - \mathbf{p}_i^{(t+1)} \right\|_2 \leq \Delta'$, holds $\forall i \in \mathcal{N}$. Here, Δ' represents an appropriate threshold that limits the power shift to prevent significant changes in the network configuration between two consecutive rounds.

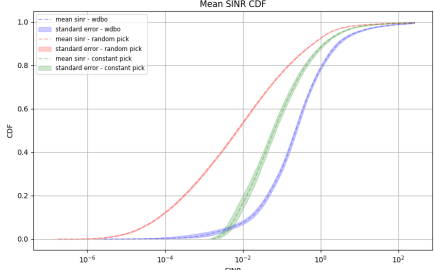
7 Conclusion

In conclusion, this work focused on developing a simulator capable of mimicking real-world dynamics to stress test the performance of the newly introduced W-DBO algorithm in power allocation decision-making for wireless cellular networks. We benchmarked the performance of W-DBO against two basic power selection strategies: Random Pick and Constant Pick. Our experiments considered three motion models of increasing complexity: Biased Random Walk, RPW, and hybrid-GMM. The results demonstrated that W-DBO consistently outperforms these simpler strategies. We also analyzed the current limitations and potential future extensions of our approach. Additionally, within the scope of motion models, we provided an explicit closed form of the hybrid-GMM motion model (Appendix A.2.2) and proposed a Custom Probabilistic Motion model that leverages available city data (Appendix A.2.1).

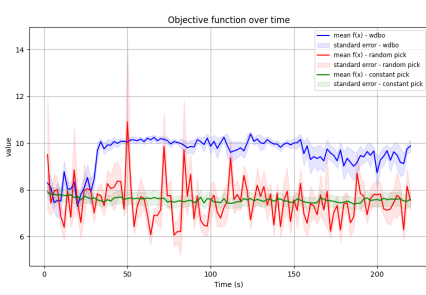
Figure 4: Comparison of W-DBO, Random pick, and Constant pick models over different mobility models (Biased Random Walk, Random Waypoint, Hybrid-GMM) with 7 replicates (except Hybrid-GMM with 8 replicates for Constant pick) and 12 BSs.



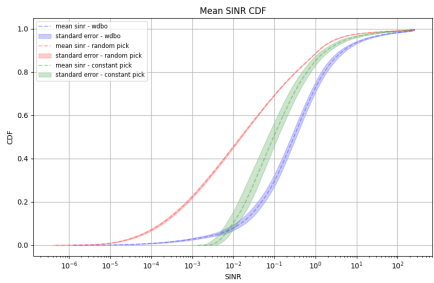
(a) Objective function comparison between W-DBO (blue), Random pick (red) and Constant pick (green). Alpha fairness equal to 1 (Biased Random Walk).



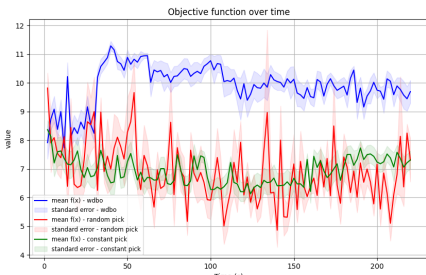
(b) SINR's cumulative distribution function comparison between W-DBO (blue), Random pick (red) and Constant pick (green). Alpha fairness equal to 1 (Biased Random Walk). A disaggregated visualization of the replicates is provided in Figure 8.



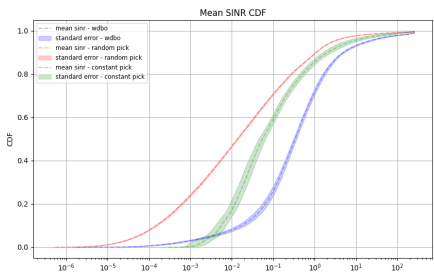
(c) Objective function comparison between W-DBO (blue), Random pick (red) and Constant pick (green). Alpha fairness equal to 1 (Random Waypoint).



(d) SINR's cumulative distribution function comparison between W-DBO (blue), Random pick (red) and Constant pick (green). Alpha fairness equal to 1 (Random Waypoint). A disaggregated visualization of the replicates is provided in Figure 10.

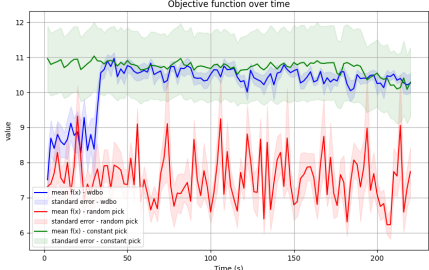


(e) Objective function comparison between W-DBO (blue), Random pick (red) and Constant pick (green). Alpha fairness equal to 1 (Hybrid-GMM).

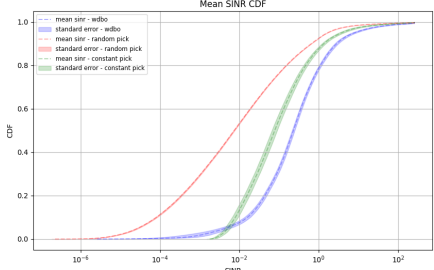


19 (f) SINR's cumulative distribution function comparison between W-DBO (blue), Random pick (red) and Constant pick (green). Alpha fairness equal to 1 (Hybrid-GMM). A disaggregated visualization of the replicates is provided in Figure 9.

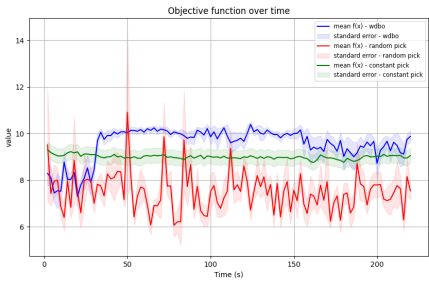
Figure 5: Comparison of W-DBO, Random pick, and Constant pick models over different mobility models (Biased Random Walk, Random Waypoint, Hybrid-GMM) with multiple replicates and 12 BSs.



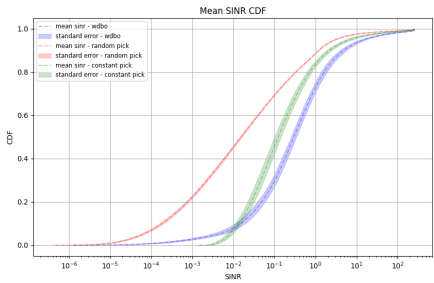
(a) Objective function comparison between W-DBO (blue - 7 replicates), Random pick (red - 14 replicates) and Constant pick (green - 18 replicates). Alpha fairness equal to 1 (Biased Random Walk).



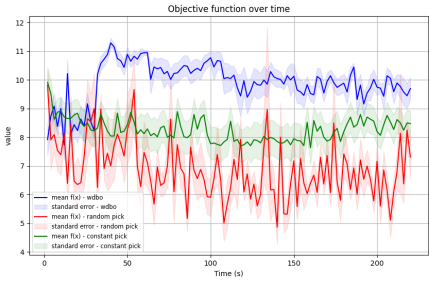
(b) SINR's cumulative distribution function comparison between W-DBO (blue - 7 replicates), Random pick (red - 14 replicates) and Constant pick (green - 18 replicates). Alpha fairness equal to 1 (Biased Random Walk).



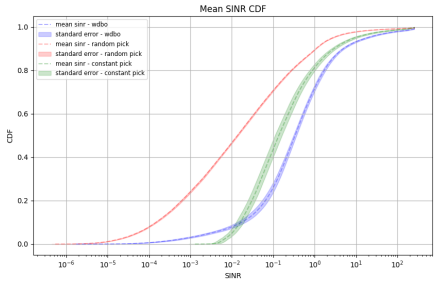
(c) Objective function comparison between W-DBO (blue - 7 replicates), Random pick (red - 7 replicates) and Constant pick (green - 19 replicates). Alpha fairness equal to 1 (Random Waypoint).



(d) SINR's cumulative distribution function comparison between W-DBO (blue - 7 replicates), Random pick (red - 7 replicates) and Constant pick (green - 19 replicates). Alpha fairness equal to 1 (Random Waypoint).

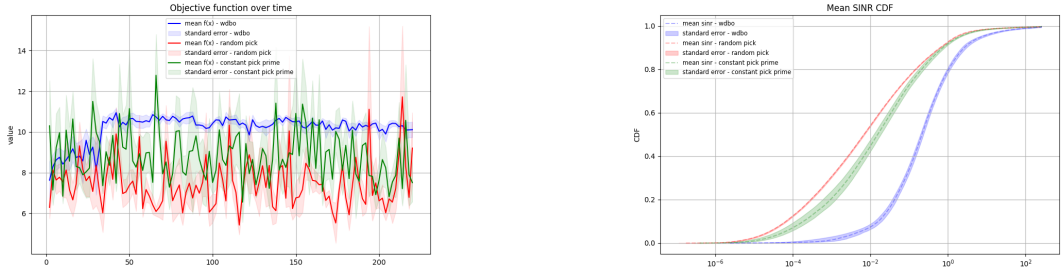


(e) Objective function comparison between W-DBO (blue - 7 replicates), Random pick (red - 7 replicates) and Constant pick (green - 17 replicates). Alpha fairness equal to 1 (Hybrid-GMM).



(f) SINR's cumulative distribution function comparison between W-DBO (blue - 7 replicates), Random pick (red - 7 replicates) and Constant pick (green - 17 replicates). Alpha fairness equal to 1 (Hybrid-GMM).

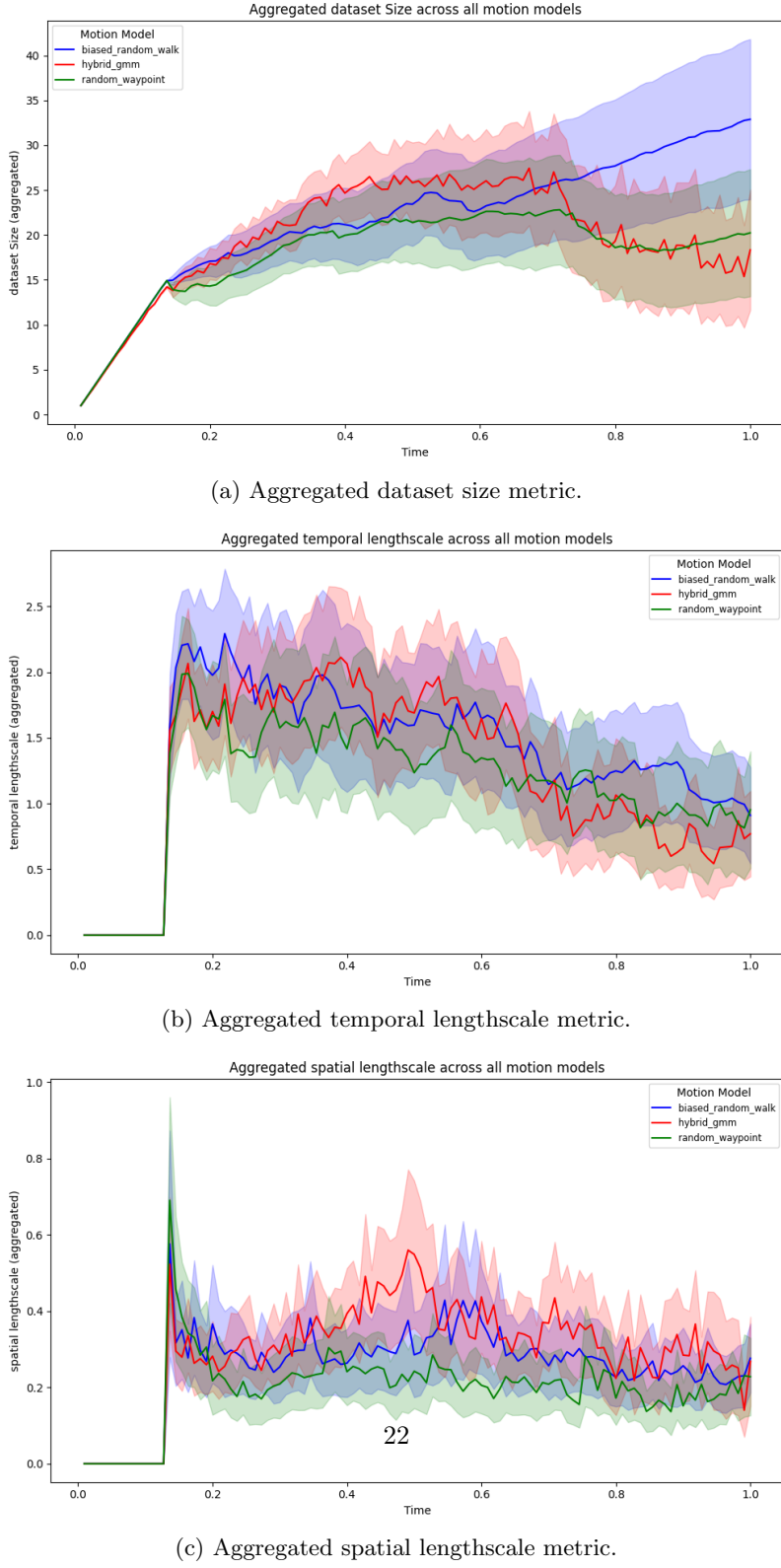
Figure 6: Comparison of W-DBO, Random pick, and Constant pick prime models over Biased Random Walk with 5 replicates and 12 BSs.



(a) Objective function comparison between W-DBO (blue), Random pick (red) and Constant pick (green). Alpha fairness equal to 1 (Biased Random Walk).

(b) SINR's cumulative distribution function comparison between W-DBO (blue), Random pick (red) and Constant pick (green). Alpha fairness equal to 1 (Biased Random Walk).

Figure 7: Aggregated metrics across 12 BSs and 7 simulation replicates. Comparison across different mobility models.



References

- [1] P. Auer. Using confidence bounds for exploitation-exploration trade-offs. *Journal of Machine Learning Research*, 3(Nov):397–422, 2002.
- [2] R. autonome des transports parisiens (RATP). Ratp data platform. <https://data.ratp.fr/explore/?sort=modified>.
- [3] F. Baccelli and B. Blaszczyszyn. *Stochastic Geometry and Wireless Networks, Volume I - Theory*, volume 1 of *Foundations and Trends in Networking Vol. 3: No 3-4, pp 249-449*. NoW Publishers, 2009. Stochastic Geometry and Wireless Networks, Volume II - Applications; see <http://hal.inria.fr/inria-00403040>.
- [4] D. Bachir, G. Khodabandou, V. Gauthier, M. El Yacoubi, and J. Puchinger. Inferring dynamic origin-destination flows by transport mode using mobile phone data. *Transportation Research Part C: Emerging Technologies*, 101:254–275, 2019.
- [5] F. Bai and A. Helmy. A survey of mobility models. *Wireless Adhoc Networks. University of Southern California, USA*, 206:147, 2004.
- [6] A. Bardou. *Online Learning for the Black-Box Optimization of Wireless Networks*. PhD thesis, École Normale Supérieure de Lyon, 2023.
- [7] A. Bardou and T. Begin. Inspire: Distributed bayesian optimization for improving spatial reuse in dense wlans. In *Proceedings of the 25th International ACM Conference on Modeling Analysis and Simulation of Wireless and Mobile Systems*, pages 133–142, 2022.
- [8] A. Bardou, P. Thiran, and T. Begin. Relaxing the additivity constraints in decentralized no-regret high-dimensional bayesian optimization. *arXiv preprint arXiv:2305.19838*, 2023.
- [9] A. Bardou, P. Thiran, and G. Ranieri. This too shall pass: Removing stale observations in dynamic bayesian optimization, 2024.
- [10] P. I. Bratanov. *User mobility modeling in cellular communications networks*. Citeseer, 1999.
- [11] T. Camp, J. Boleng, and V. Davies. A survey of mobility models for ad hoc network research. *Wireless communications and mobile computing*, 2(5):483–502, 2002.
- [12] B. Clerckx, Y. Mao, R. Schober, E. A. Jorswieck, D. J. Love, J. Yuan, L. Hanzo, G. Y. Li, E. G. Larsson, and G. Caire. Is noma efficient in multi-antenna networks? a critical look at next generation multiple access techniques. *IEEE Open Journal of the Communications Society*, 2:1310–1343, 2021.
- [13] M. Coupechoux. Ofdma cellular access and lte. <https://marceaucoupechoux.wp.imt.fr/files/2021/02/08-ofdmacellularaccess.pdf>, 2021.

- [14] B. Dybiec, E. Gudowska-Nowak, E. Barkai, and A. A. Dubkov. Lévy flights versus lévy walks in bounded domains. *Physical Review E*, 95(5):052102, 2017.
- [15] Y. C. Eldar, A. Goldsmith, D. Gündüz, and H. V. Poor. *Machine learning and wireless communications*. Cambridge University Press, 2022.
- [16] M. Ester, H.-P. Kriegel, J. Sander, X. Xu, et al. A density-based algorithm for discovering clusters in large spatial databases with noise. In *kdd*, volume 96, pages 226–231, 1996.
- [17] N. Ferreira, J. Poco, H. T. Vo, J. Freire, and C. T. Silva. Visual exploration of big spatio-temporal urban data: A study of new york city taxi trips. *IEEE transactions on visualization and computer graphics*, 19(12):2149–2158, 2013.
- [18] France Government. Arcep Mobile Data - Base station sites. https://files.data.gouv.fr/arcep_donnees/mobile/sites/2022_T3/2022_T3_sites_Metropole.csv, 2022.
- [19] R. Garnett. *Bayesian optimization*. Cambridge University Press, 2023.
- [20] X. Ge, J. Ye, Y. Yang, and Q. Li. User mobility evaluation for 5g small cell networks based on individual mobility model. *IEEE Journal on Selected Areas in Communications*, 34(3):528–541, 2016.
- [21] M. C. Gonzalez, C. A. Hidalgo, and A.-L. Barabasi. Understanding individual human mobility patterns. *nature*, 453(7196):779–782, 2008.
- [22] J.-M. Gorce, P. Mary, D. Anade, and J.-M. Kélib. Fundamental limits of non-orthogonal multiple access (noma) for the massive gaussian broadcast channel in finite block-length. *Sensors*, 21(3):715, 2021.
- [23] Z. Huang, X. Ling, P. Wang, F. Zhang, Y. Mao, T. Lin, and F.-Y. Wang. Modeling real-time human mobility based on mobile phone and transportation data fusion. *Transportation research part C: emerging technologies*, 96:251–269, 2018.
- [24] J. D. Hunter. Matplotlib: A 2d graphics environment. *Computing in Science & Engineering*, 9(3):90–95, 2007.
- [25] E. Hyytiä and J. Virtamo. Random waypoint mobility model in cellular networks. *Wireless Networks*, 13(2):177–188, 2007.
- [26] S. Isaacman, R. Becker, R. Cáceres, M. Martonosi, J. Rowland, A. Varshavsky, and W. Willinger. Human mobility modeling at metropolitan scales. In *Proceedings of the 10th international conference on Mobile systems, applications, and services*, pages 239–252, 2012.
- [27] K. K. Jahromi, M. Zignani, S. Gaito, and G. P. Rossi. Simulating human mobility patterns in urban areas. *Simulation Modelling Practice and Theory*, 62:137–156, 2016.

- [28] C. Jiang, H. Zhang, Y. Ren, Z. Han, K.-C. Chen, and L. Hanzo. Machine learning paradigms for next-generation wireless networks. *IEEE Wireless Communications*, 24(2):98–105, 2016.
- [29] D. R. Jones, M. Schonlau, and W. J. Welch. Efficient global optimization of expensive black-box functions. *Journal of Global optimization*, 13:455–492, 1998.
- [30] L. V. Kantorovich. Mathematical methods of organizing and planning production. *Management science*, 6(4):366–422, 1960.
- [31] O. Kiss. arxiv: Bayesian optimization for machine learning algorithms in the context of higgs searches at the cms experiment. Technical report, 2019.
- [32] R. C. Kizilirmak and H. K. Bizaki. Non-orthogonal multiple access (noma) for 5g networks. *Towards 5G wireless networks-a physical layer perspective*, 83:83–98, 2016.
- [33] R. C. Kizilirmak and H. K. Bizaki. Non-orthogonal multiple access (noma) for 5g networks. *Towards 5G Wireless Networks-A Physical Layer Perspective*, 83:83–98, 2016.
- [34] L. Kleinrock. Queuing systems, volume i: Theory, 1975.
- [35] D. Krajzewicz, G. Hertkorn, C. Rössel, and P. Wagner. Sumo (simulation of urban mobility)-an open-source traffic simulation. In *Proceedings of the 4th middle East Symposium on Simulation and Modelling (MESM20002)*, pages 183–187, 2002.
- [36] B. Liang and Z. J. Haas. Predictive distance-based mobility management for multidimensional pcs networks. *IEEE/ACM Transactions On Networking*, 11(5):718–732, 2003.
- [37] X. Lin, R. K. Ganti, P. J. Fleming, and J. G. Andrews. Towards understanding the fundamentals of mobility in cellular networks. *IEEE Transactions on Wireless Communications*, 12(4):1686–1698, 2013.
- [38] X. Lin, R. K. Ganti, P. J. Fleming, and J. G. Andrews. Towards understanding the fundamentals of mobility in cellular networks. *IEEE Transactions on Wireless Communications*, 12(4):1686–1698, 2013.
- [39] A. Loder, L. Ambühl, M. Menendez, and K. W. Axhausen. Understanding traffic capacity of urban networks. *Scientific reports*, 9(1):16283, 2019.
- [40] A. Loder, L. Ambühl, M. Menendez, and K. W. Axhausen. Utd19: Understanding traffic capacity of urban networks. 2020.
- [41] J. MacQueen et al. Some methods for classification and analysis of multivariate observations. In *Proceedings of the fifth Berkeley symposium on mathematical statistics and probability*, volume 1, pages 281–297. Oakland, CA, USA, 1967.

- [42] R. N. Mantegna. Fast, accurate algorithm for numerical simulation of levy stable stochastic processes. *Physical Review E*, 49(5):4677, 1994.
- [43] R. N. Mantegna and H. E. Stanley. Stochastic process with ultraslow convergence to a gaussian: the truncated lévy flight. *Physical Review Letters*, 73(22):2946, 1994.
- [44] R. N. Mantegna and H. E. Stanley. Scaling behaviour in the dynamics of an economic index. *Nature*, 376(6535):46–49, 1995.
- [45] H. Martin, Y. Hong, N. Wiedemann, D. Bucher, and M. Raubal. Trackintel: An open-source python library for human mobility analysis. *Computers, Environment and Urban Systems*, 101:101938, 2023.
- [46] M. McIntire, D. Ratner, and S. Ermon. Sparse gaussian processes for bayesian optimization. In *UAI*, volume 3, page 4, 2016.
- [47] J. Mo and J. Walrand. Fair end-to-end window-based congestion control. *IEEE/ACM Transactions on networking*, 8(5):556–567, 2000.
- [48] J. Mockus. Application of bayesian approach to numerical methods of global and stochastic optimization. *Journal of Global Optimization*, 4:347–365, 1994.
- [49] J. Møller, A. R. Syversveen, and R. P. Waagepetersen. Log gaussian cox processes. *Scandinavian journal of statistics*, 25(3):451–482, 1998.
- [50] U. of Bonn. A mobility scenario generation and analysis tool. <https://net.cs.uni-bonn.de/wg/cs/applications/bonnmotion/>.
- [51] C. of Paris. Paris' open data platform. <https://opendata.paris.fr/pages/home/>.
- [52] OpenStreetMap contributors. Planet dump retrieved from <https://planet.osm.org> . <https://www.openstreetmap.org>, 2017.
- [53] A. Pani遧on. Pymobility v0. 1—python implementation of mobility models, 2014.
- [54] L. Pappalardo, F. Simini, G. Barlacchi, and R. Pellungrini. scikit-mobility: A python library for the analysis, generation and risk assessment of mobility data. *arXiv preprint arXiv:1907.07062*, 2019.
- [55] python visualization. Folium.
- [56] A. Sankararaman and F. Baccelli. Spatial birth–death wireless networks. *IEEE Transactions on Information Theory*, 63(6):3964–3982, 2017.
- [57] K. Sato and K. Suto. Bayesian optimization framework for channel simulation-based base station placement and transmission power design. *arXiv preprint arXiv:2407.20778*, 2024.

- [58] S. Sen, N. Santhapuri, R. R. Choudhury, and S. Nelakuditi. Successive interference cancellation: A back-of-the-envelope perspective. In *Proceedings of the 9th ACM SIGCOMM Workshop on Hot Topics in Networks*, pages 1–6, 2010.
- [59] F. Simini, M. C. González, A. Maritan, and A.-L. Barabási. A universal model for mobility and migration patterns. *Nature*, 484(7392):96–100, 2012.
- [60] J. Snoek, O. Rippel, K. Swersky, R. Kiros, N. Satish, N. Sundaram, M. M. A. Patwary, Prabhat, and R. P. Adams. Scalable bayesian optimization using deep neural networks, 2015.
- [61] N. Srinivas, A. Krause, S. M. Kakade, and M. W. Seeger. Information-theoretic regret bounds for gaussian process optimization in the bandit setting. *IEEE transactions on information theory*, 58(5):3250–3265, 2012.
- [62] L. Sun and K. W. Axhausen. Understanding urban mobility patterns with a probabilistic tensor factorization framework. *Transportation Research Part B: Methodological*, 91:511–524, 2016.
- [63] Y. Sun, M. Peng, Y. Zhou, Y. Huang, and S. Mao. Application of machine learning in wireless networks: Key techniques and open issues. *IEEE Communications Surveys & Tutorials*, 21(4):3072–3108, 2019.
- [64] M. W. Traunmueller, N. Johnson, A. Malik, and C. E. Kontokosta. Digital footprints: Using wifi probe and locational data to analyze human mobility trajectories in cities. *Computers, Environment and Urban Systems*, 72:4–12, 2018.
- [65] S. Uppoor, O. Trullols-Cruces, M. Fiore, and J. M. Barcelo-Ordinas. Generation and analysis of a large-scale urban vehicular mobility dataset. *IEEE Transactions on Mobile Computing*, 13(5):1061–1075, 2013.
- [66] Website. Lte physical layer overview. https://helpfiles.keysight.com/csg/89600B/Webhelp/Subsystems/lte/content/lte_overview.htm.
- [67] C. Williams and C. Rasmussen. Gaussian processes for regression. *Advances in neural information processing systems*, 8, 1995.
- [68] X.-Y. Yan, C. Zhao, Y. Fan, Z. Di, and W.-X. Wang. Universal predictability of mobility patterns in cities. *Journal of The Royal Society Interface*, 11(100):20140834, 2014.
- [69] S. Yang, B. Liu, Z. Hong, and Z. Zhang. Bayesian optimization-based beam alignment for mmwave mimo communication systems. In *2022 IEEE 33rd Annual International Symposium on Personal, Indoor and Mobile Radio Communications (PIMRC)*, pages 825–830. IEEE, 2022.

- [70] D. Zhang, J. Zhao, F. Zhang, and T. He. Urbancps: A cyber-physical system based on multi-source big infrastructure data for heterogeneous model integration. In *Proceedings of the ACM/IEEE Sixth International Conference on Cyber-Physical Systems*, pages 238–247, 2015.
- [71] Île-de France Mobilités. Île-de-france mobilités open data. <https://data.iledefrance-mobilites.fr/pages/home/>.

A Appendix

A.1 User Generation

A.1.1 Radial-basis distribution

If data are available, the initial pool of users can be placed in the grid according to the distribution associated with the normalized traffic flow ζ . Alternatively, ζ can be estimated through a normalized radial-basis density distribution. Let I represent a partition of the grid Ω , defining a disjointed set of square tiles. We denote the coordinates of a specific grid tile ι by $\delta(\iota)$ and the coordinates of the center by $\delta(\kappa)$, where $\delta(\cdot) \in \mathbb{R}^2$.

Then,

$$\mathbb{P}(s = \iota) = \frac{e^{-\|\delta(\iota) - \delta(\kappa)\|_2^2}}{\sum_{\iota \in \Omega} e^{-\|\delta(\iota) - \delta(\kappa)\|_2^2}} \quad (18)$$

This follows the assumption that urban density decreases as the distance from the urban center increases. The notion of an urban center indicates the point in space where urban density reaches its peak, and might not coincide with the geometric centroid of the grid. It can be estimated by analyzing the density of BSs within a neighborhood of a given radius or considering the traffic flow. In our scenario, the center is defined as follows:

$$\begin{aligned} \delta(\kappa) &= \operatorname{argmax}_{\alpha \in \Omega} \lim_{r \rightarrow 0} |\mathcal{B}(\alpha, r)| \\ &\text{s.t.} \\ &|\mathcal{B}(\alpha, r)| > 1 \\ &\alpha \in \mathbb{R}^2 \end{aligned} \quad (19)$$

Let Z be the set of BSs within the grid, and let $\mathcal{B}(\alpha, r)$ be the ball encompassing the base stations that lie in its area. Let the operator “ $|\cdot|$ ” extend the notion of set cardinality to the ball, indicating the number of base stations within the ball. Thus:

$$\mathcal{B}(\alpha, r) = \{z \in Z : \|\delta(z) - \alpha\|_2 \leq r\} \quad (20)$$

The analysis can be extended to a multi-center setting, where $\kappa = (\kappa_1, \dots, \kappa_{\tilde{M}})$, with \tilde{M} denoting the cardinality of the multicenter set. In this case, a Gaussian Mixture can be used to model UEs generation, accounting for dispersion around multiple meaningful points.

A.2 Mobility models

A.2.1 Custom Probabilistic Mobility Model

The proposed probabilistic model is built as follows:

$X^{(j)} = \{\nu^{(j)}\}_{t^{(j)}=1}^{T^{(j)}}$ being the trajectory for the j -th user, such that $j \in \mathcal{M}$, where \mathcal{M} is the set of

users. Each user j has a total lifetime in the system indicated as $T^{(j)}$. Let $\{u_h\}_{h=1}^H$ be the set of means of transport. The area of interest is denoted as Ω , where ι denotes the ι -th section (please refer to the partition specified in Section A.1.1), such that $\bigcup_{\iota \in \Omega} \iota = \Omega$ and $\bigcap_{\iota \in \Omega} \iota = \emptyset$, to ensure partition properties, $\iota \in \mathbb{N}$. For the purpose of our model, each ι corresponds to a tile of the grid. We can formulate transitions as follows:

$$\begin{aligned}\nu_{t+1}^{*(j)} &= \operatorname{argmax}_{\iota' \in \Omega_\iota} \mathbb{P} \left(\nu_{t+1}^{(j)} = \iota', \nu_t^{(j)} = \iota \right) \\ &= \operatorname{argmax}_{\iota' \in \Omega_\iota} \mathbb{P} \left(\nu_{t+1}^{(j)} = \iota' \mid \nu_t^{(j)} = \iota \right) \mathbb{P} \left(\nu_t^{(j)} = \iota \right)\end{aligned}\quad (21)$$

Such that $\Omega_\iota = \bigcup_{h=1}^H \Omega_{\iota,h}$ and $\Omega_{\iota,h} = \{\iota' \in \Omega \mid \iota' = \iota + \vec{v}_h\}$. Let \vec{v}_h be average velocity associated with the h -th mean of transport, so that $\vec{v}_h = \vec{v}_h^{(t)}$, $t = 1, \dots, \bigcup_{j \in \mathcal{M}} T^{(j)}$ (Without loss of generality it is assumed that $\min_{j \in \mathcal{M}} t^{(j)} = 1$).

A logical approximation derives from considering a trajectory constrained by the choice of the mean of transport, both in terms of speed and reachable sector, due to infrastructure placement and ramifications. In fact, in realistic scenarios, travel flows are dependent on the type of road, rails, or more generally, traffic limitations in place. Thus, by considering displacement strictly dependent on the mode of transport, we could express the transition probability as follows:²

$$\begin{aligned}\mathbb{P} \left(\nu_{t+1}^{(j)} = \iota' \mid \nu_t^{(j)} = \iota \right) \mathbb{P} \left(\nu_t^{(j)} = \iota \right) &= \\ \sum_{h=1}^H \mathbb{P} \left(u_{h,\iota',t+1}^{(j)} \mid u_{h,\iota,t}^{(j)} \right) \mathbb{P} \left(u_{h,\iota,t}^{(j)} \right) &\end{aligned}\quad (22)$$

To the extent of our analysis, let the symbol “ \dashv ” denote the operator that generalized the notion of *belonging* in non-mathematical sense, i.e. it indicates the means of transport passing through a tile or the user being on a given means of transport. Let $\mathbb{P} \left(u_{h,\iota,t}^{(j)} \right) = \mathbb{P} \left(j \dashv u_h, u_h \dashv \iota, \nu_t^{(j)} = \iota \right)$, such that:

$$\begin{aligned}\mathbb{P} \left(j \dashv u_h, u_h \dashv \iota, \nu_t^{(j)} = \iota \right) &= \\ \mathbb{P} \left(j \dashv u_h \mid u_h \dashv \iota, \nu_t^{(j)} = \iota \right) \mathbb{P} \left(u_h \dashv \iota, \nu_t^{(j)} = \iota \right) &\end{aligned}\quad (23)$$

Due to independence, $\mathbb{P} \left(u_h \dashv \iota, \nu_t^{(j)} = \iota \right) = \mathbb{P} \left(u_h \dashv \iota \right) \mathbb{P} \left(\nu_t^{(j)} = \iota \right)$.

To simplify the model without losing interpretability, we could consider that on a given tile, for a given destination, users choose the means of transport based on the highest availability, which in our model embeds the notion of time to reach the destination and passing frequency. Thus, $\mathbb{P} \left(u_{h,\iota',t+1}^{(j)} \mid u_{h,\iota,t}^{(j)} \right) \approx \mathbb{P} \left(u_{h,\iota',t+1}^{(j)} \right)$. Furthermore, $\mathbb{P} \left(\nu_t^{(j)} = \iota \right)$ is computed considering the normalized average traffic flow density, i.e., people/ m^2 , of a given sector, obtained from the city's available data. Since it only provides a snapshot at a given time and not the entire real-time time

²Marginalizing by u_h implies that we do not need to take into account the user choice, as we naively assume the user takes the most available means of transportation. This defines an upper bound over the real case, where there is a higher degree of randomness in the user mobility choices.

series of the available traffic flow, we can approximate this probability as stationary in time and independent of the user. Therefore, $\mathbb{P}(\nu_t^{(j)} = \iota) = \mathbb{P}(\nu = \iota), t = 1, \dots, \bigcup_{j \in \mathcal{M}} T^{(j)}$, which implies that $\mathbb{P}(u_{h,\iota,t}^{(j)}) = \mathbb{P}(u_{h,\iota}), t = 1, \dots, \bigcup_{j \in \mathcal{M}} T^{(j)}$.

Let ζ denote state probability vector, such that $\zeta_i = \mathbb{P}(\nu = \iota)$. To ease notation, let $I = |\Omega|$, and let $U = \mathbb{P}(u_{h,\iota})_{h=1, \dots, H; \iota=1, \dots, I}$ be the $H \times I$ matrix that maps the joint distribution of urban transport means and user location on the grid in probabilistic terms. Also, let $W = \mathbb{P}(u_h \dashv \iota)_{h=1, \dots, H; \iota=1, \dots, I}$, and $\theta^{(j)} = \mathbb{P}(j \dashv u_h | \cdot)_{h=1, \dots, H} \sim \mathcal{U}(1, H)$, being \mathcal{U} a uniform distribution. By assuming users to be IID on the transportation choice, $\theta^{(j)} = \theta, \forall j \in \mathcal{M}$.

We can then reduce our problem to an algebraic form as follows:

$$\nu_{t+1}^{*(j)} = \operatorname{argmax}_{\iota' \in \Omega_\iota} U_{\iota'}^\top U_\iota = \operatorname{argmax} U^\top U \quad (24)$$

$$U = \theta \zeta^\top \otimes W \quad (25)$$

Where “ \otimes ” denotes the element-wise product and $(\cdot)^\top$ indicates the transpose operation. Therefore, the trajectory for the j -th user can be expressed as:

$$X^{(j)} = \{\operatorname{argmax} U^\top U_{\nu_{t-1}}\}_{t=1}^{T^{(j)}} \quad (26)$$

Where $\nu_0^{(j)}$ is the user's spawning tile.

The following databases provide insights regarding urban flow in the city of Paris: [40, 51, 71, 2].

A.2.2 hybrid-GMM Equations

Given H clusters and \mathcal{M} users, such that $j_h \in \mathcal{M}$ is the j -th user that belongs to the h -th cluster. We define the following notions:

- $\delta(\cdot) : \Omega \rightarrow \mathbb{R}^2$: the coordinates function.
- $\vec{\delta}(\cdot) \in \mathbb{R}^2$: the vector associated with a point in the space.
- $\alpha_h = \mathcal{U}(0.1, 1)$: the momentum parameter associated with a cluster motion, sampled from a uniform distribution.
- σ'_h : standard deviation parameter to regulate the degree of randomness in cluster h motion.
- $\beta_h = \sigma'_h \sqrt{1 - \alpha_h^2}$.
- $\vec{v}_h^{(t)} \in \mathbb{R}^2$: the velocity of the h -th cluster at time-step t .
- $d_h^{(t)} = \mathcal{U}(\Xi)$: the destination, sampled from the destinations set Ξ , that is aimed at time-step t .

- $\delta(\nu_h^{(t)}) = (x_h^{(t)}, y_h^{(t)})$: cluster h centroid position at time-step t , where $\{\nu_h^{(t)}\}_{t=1}^T$ is the trajectory of the cluster w.r.t the grid tiles.
- $\lambda_h^{(t)} = \tan^{-1} \left(\frac{\delta(d_h^{(t)})_2 - y_h^{(t)}}{\delta(d_h^{(t)})_1 - x_h^{(t)}} \right)$.
- $\vec{h}_{avg,h}$: average velocity vector for cluster h .

Motion Update

$$x_h^{(t+1)} = x_h^{(t)} + \vec{v}_{h,1}^{(t)} \cdot \cos(\theta_h^{(t)}) \quad (27)$$

$$y_h^{(t+1)} = y_h^{(t)} + \vec{v}_{h,2}^{(t)} \cdot \sin(\theta_h^{(t)}) \quad (28)$$

$$\theta_h^{(t+1)} = \alpha_h \theta_h^{(t)} + (1 - \alpha_h) \lambda_h^{(t)} + \beta_h \mathcal{U}(0, 1) \quad (29)$$

$$\vec{v}_h^{(t+1)} = \alpha_h \vec{v}_h^{(t)} + (1 - \alpha_h) \vec{v}_{avg,h} + \beta_h \mathcal{U}(0, 1) \quad (30)$$

(31)

$$\begin{aligned} & \text{if } \left\| \vec{\delta}(\nu_h^{(t)}) - \vec{\delta}(d_h^{(t)}) \right\|_2 < \psi \\ & \text{then } d_h^{(t+1)} = \mathcal{U}(\Xi \setminus d_h^{(t)}) \\ & \text{else } d_h^{(t+1)} = d_h^{(t)} \end{aligned} \quad (32)$$

Where ψ is an arbitrary small value.

A.3 Experimental testbed

A.3.1 Computational time comparison

Table 1: Computational Time Comparison

Method	Approximate W-DBO Time	Approximate Pick Time (Random, Constant)
Biased Random Walk	85-90 mins	35-40 mins
Random-waypoint	85-90 mins	35-40 mins
Hybrid-GMM	85-90 mins	35-40 mins

A.3.2 Visual representations

Interactive graphic visualizations are accessible in the following folder: NOMA Simulator - Visualizations.

For each of the tested motion models, four GIF-based visualizations are provided: two using the *matplotlib* library [24] and two using *folium* [55] and [52]. Specifically, the representation tagged as *voronoi*_ defines a cell-breathing representation, showing the evolution of the inner and outer areas of a given BS. Additionally, the red rectangle delineates the set of BSs retained for the performance

analysis, i.e., those not subject to border filtering. The other two visualizations offer a simpler and cleaner depiction of the network, intended to highlight the motion dynamics. To correctly load the *matplotlib* GIF visualizations on a local device, please download the corresponding frames folder.

A.3.3 Hyper-parameters of the Simulator - 12 BSs

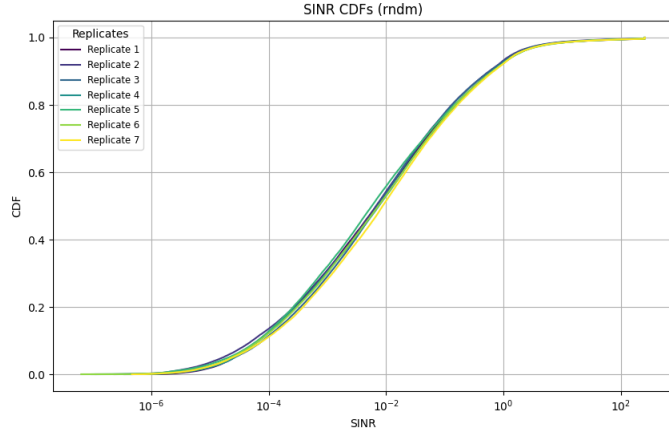
Parameter	Value/Range	Description
General Simulation		
Origin coordinates reference	(48.839509321605924, 2.2541463716478995)	
Simulation Step	1 s	Time step for the simulation
Simulation Time	220s/110 optimization rounds	Total simulation time duration
Network Width	2.4 km (Paris sub-area)	Width of the network area
Network Height	1.1 km (Paris sub-area)	Height of the network area
Tile Size	25 m	Size of each tile side in the grid
Translation interval	2s	Move interval and metrics collection interval
λ	1/3	UEs' arrival rate for Poisson process - birth
μ	1/10	Rate for UEs' lifetime exponential distribution - death
UEs placement seed	21	
Motion seed	42	
B&D seed	30	
User Equipment (UE) Generation		
User Coordinates	$\mathcal{U}(\Omega) \in \mathbb{R}^2$	Distribution for users coordinates
User velocity domain	[3.06, 19.8] km/h	
Biased Random Walk		
bias-direction	$\mathcal{U}(0, 2\pi)$	Sampled every 25 iterations
bias-strength	$\mathcal{U}(0.3, 0.7)$	Sampled every 25 iterations
Velocity	$\mathcal{U}(3.06, 19.8)$	
sampled at each round Random Direction (θ)	$\mathcal{U}(0, 2\pi)$	Sampled at each iteration
Levy Walk		
α	1	
Step size	[42] procedure	
Direction (θ)	$\mathcal{U}(0, 2\pi)$	Sampled at each iteration
Truncated Levy Walk		
max_step_length	25m (tile size)	
α	1	Capped with max_step_length
Step size	[42] procedure	
Direction (θ)	$\mathcal{U}(0, 2\pi)$	Sampled at each iteration
Brownian motion		
α	2	
Step size	[42] procedure	
Direction (θ)	$\mathcal{U}(0, 2\pi)$	Sampled at each iteration
Random Waypoint		
wt_max	1	Maximum number of waiting steps
Hybrid-GMM		
K-Means Clusters (random state 56)	$nc = 20$	Number of clusters for K-Means, applied to the first set of UEs
DBSCAN	eps=300m, min_samples=1, "euclidian" distance	Settings for DBSCAN clustering on BSs dataset to retrieve way-points
Destination Set Ξ	DBSCAN clusters from BSs dataset	Set of possible destinations
MC Sample Size (mc)	1000	Number of Monte Carlo samples
Cluster Average Velocity	$\sum_1^{mc} \mathcal{U}(3.06, 19.8)/mc$ km/h	Average velocity of a cluster
α	$\mathcal{U}(0.1, 1)$	Momentum factor for motion
Cluster Variance (σ')	$\mathcal{U}(0.5, 1.5)$	Variance in cluster movement
Cluster Way-point	$\mathcal{U}(\Xi)$	Random cluster destination
ψ	0.3 km	Destination closeness criterion
ϵ	0.3	Greedy factor for determining cluster's pause
UE Position After Motion	$\mathcal{U}(\mathcal{B}(\mu'_c, 100)$	Uniformly distributed around cluster centroid $\mu'_c \in \mathbb{R}^2$
Base Station (BS)		
Number of BSs	12	BSs areal density 4.55
Bandwidth	20 MHz	Operational bandwidth
Reference Path Loss	120 dBm at 1km	Initial path loss at 1 kilometer
Nominal Transmit Power (P_{tx})	46 dBm	Nominal transmit power
Minimum Transmit Power (P_{tx}^{min})	10 dBm	
Noise Density	-125 dBm/Hz	Ambient noise density
Shadowing (X_g)	0	Shadowing effect
Path Loss Exponent	3.76	Path loss exponent, variable
Nominal Coverage	470 m	Nominal coverage of a base station
Border filter	200m	
WDBO Optimizer ([9])		
n_initial_observations	15	Number of initial observation for the WDBO optimizer
spatial_kernel_args	(2.5)	Used in WDBO criterion
temporal_kernel_args	(1.5)	Used in WDBO criterion

Table 2: List of hyperparameters set by the user or sampled from a distribution in the simulator.

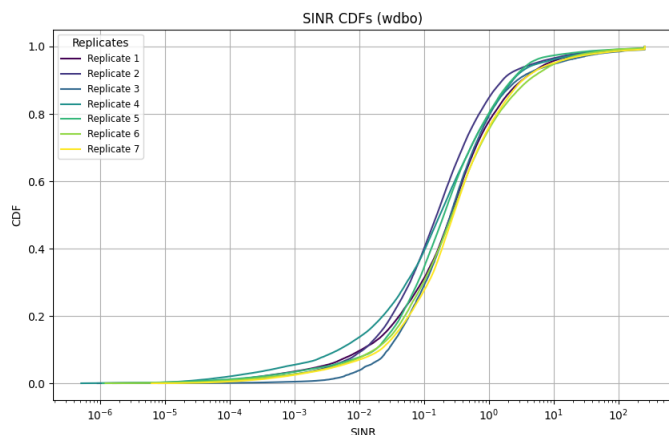
A.4 Results' extended visualizations

A.4.1 SINRs' CDFs comparison

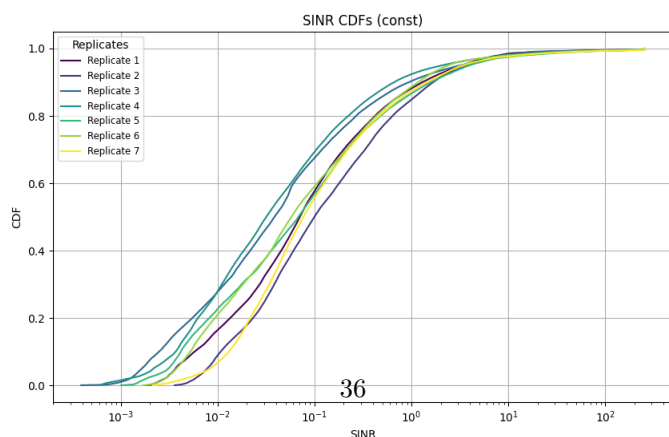
Figure 8: SINR CDFs' comparison over replicates, biased random walk.



(a) Random Pick SINR CDF over replicates, biased random walk.

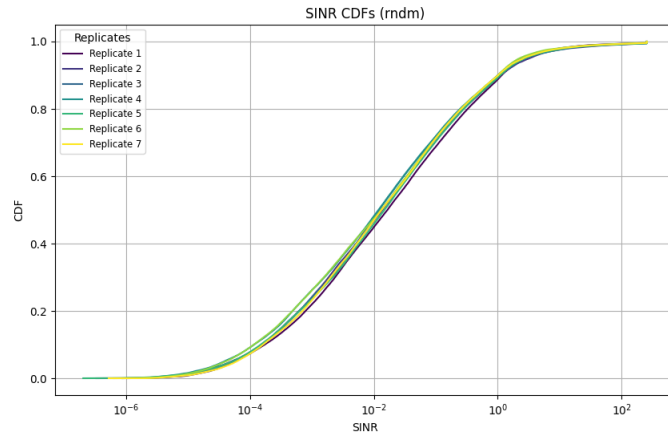


(b) W-DBO SINR CDF over replicates, biased random walk.

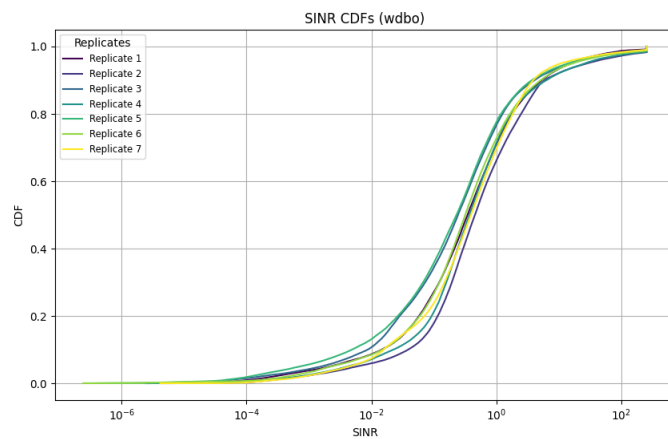


(c) Constant Pick SINR CDF over replicates, biased random walk.

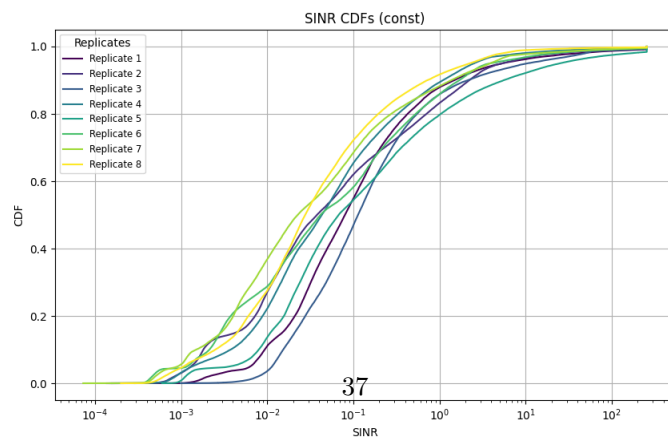
Figure 9: SINR CDFs' comparison over replicates, hybrid-gmm.



(a) Random Pick SINR CDF over replicates, hybrid-gmm.



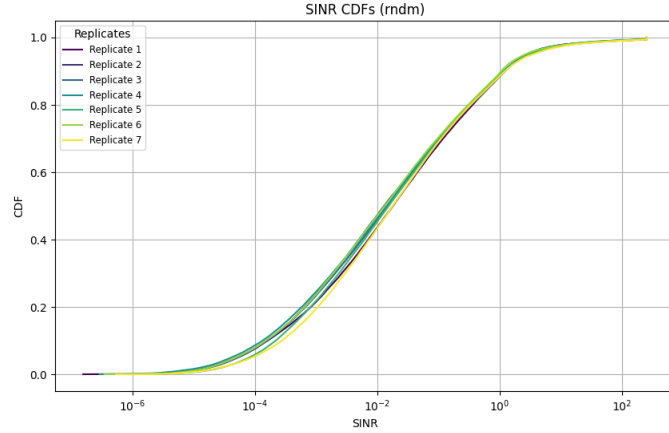
(b) W-DBO SINR CDF over replicates, hybrid-gmm.



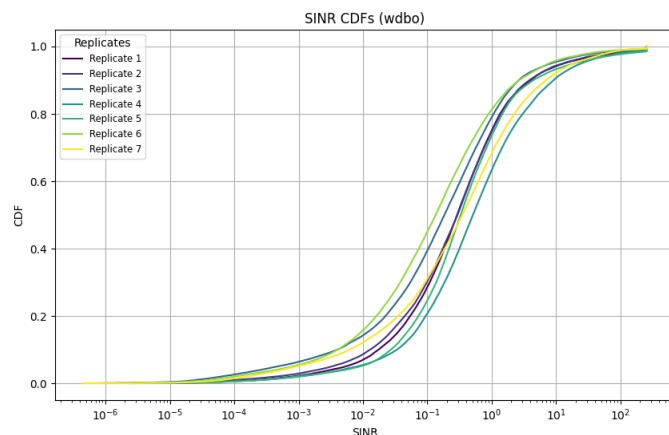
37

(c) Constant Pick SINR CDF over replicates, hybrid-gmm.

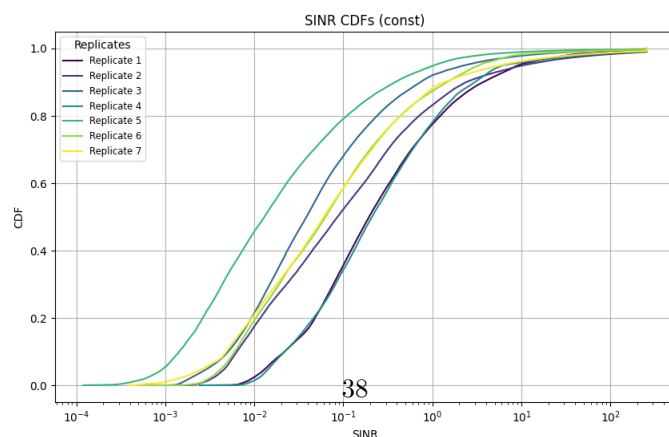
Figure 10: SINR CDFs' comparison over replicates, random waypoint.



(a) Random Pick SINR CDF over replicates, random waypoint.



(b) W-DBO SINR CDF over replicates, random waypoint.



(c) Constant Pick SINR CDF over replicates, random waypoint.

A.4.2 W-DBO's hyper-parameters comparison, aggregation by replicates

Figure 11: Dataset size vs. time across different mobility models. Aggregation of 7 replicates. Each subfigure shows the dataset size variation over time for a specific mobility model.

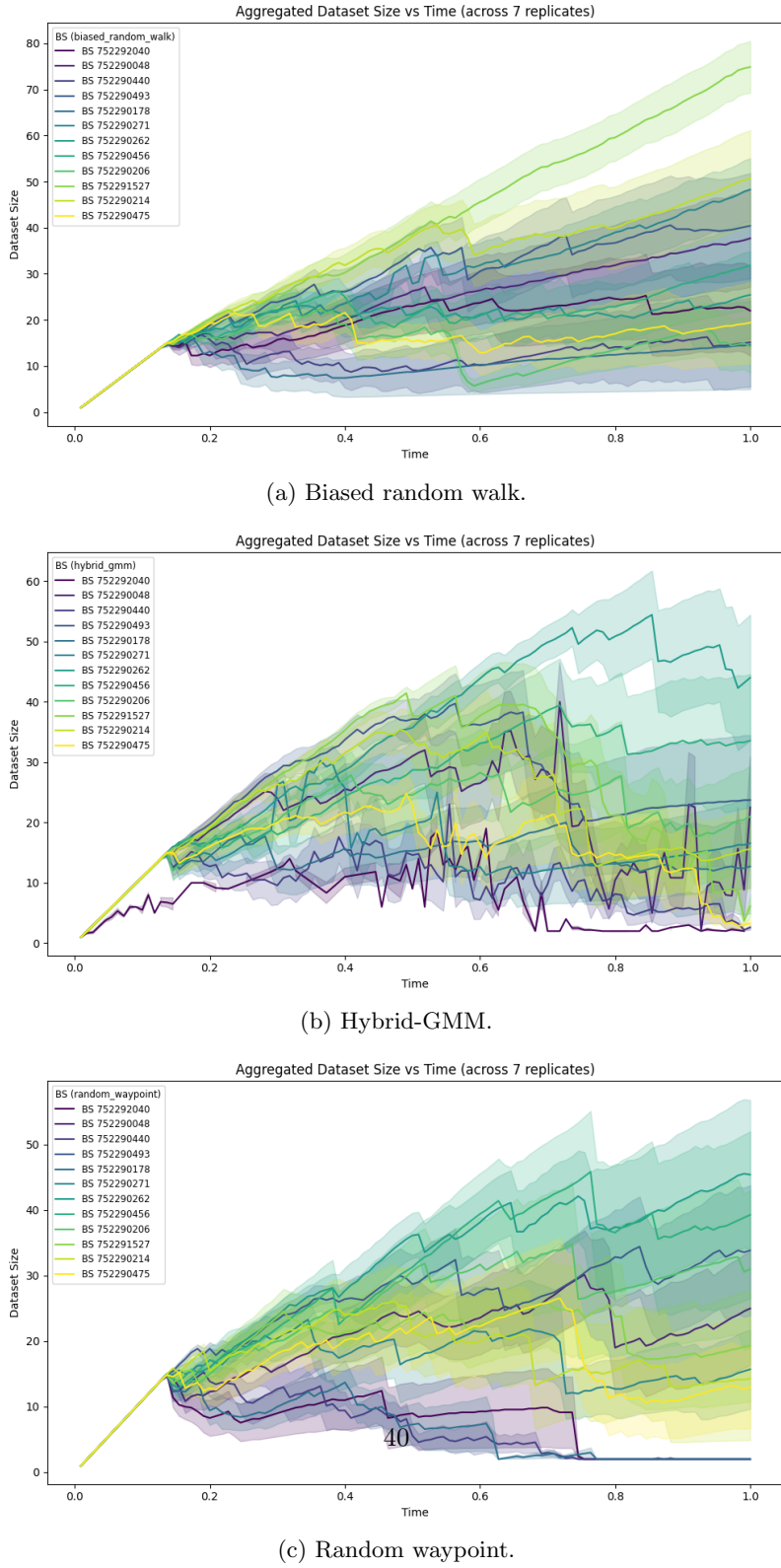


Figure 12: Temporal lengthscale vs. time across different mobility models. Aggregation of 7 replicates. Each subfigure shows the temporal lengthscale variation over time for a specific mobility model.

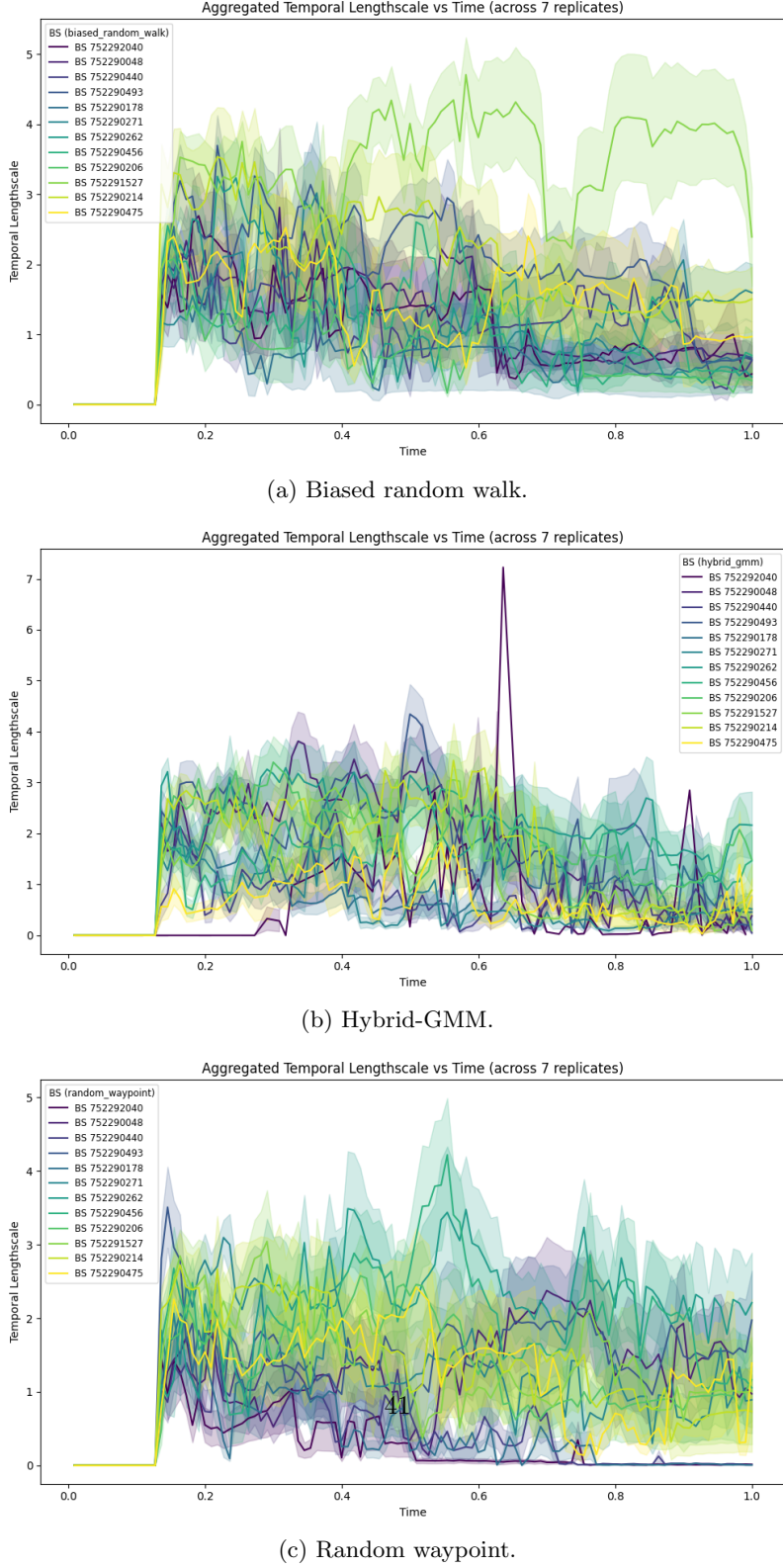
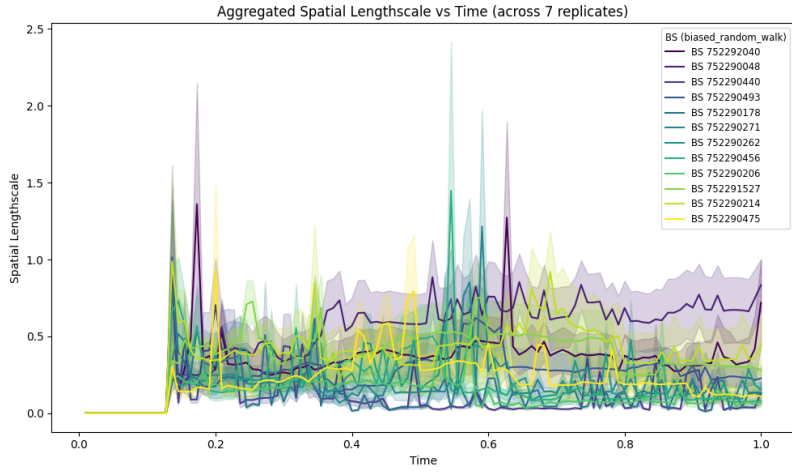
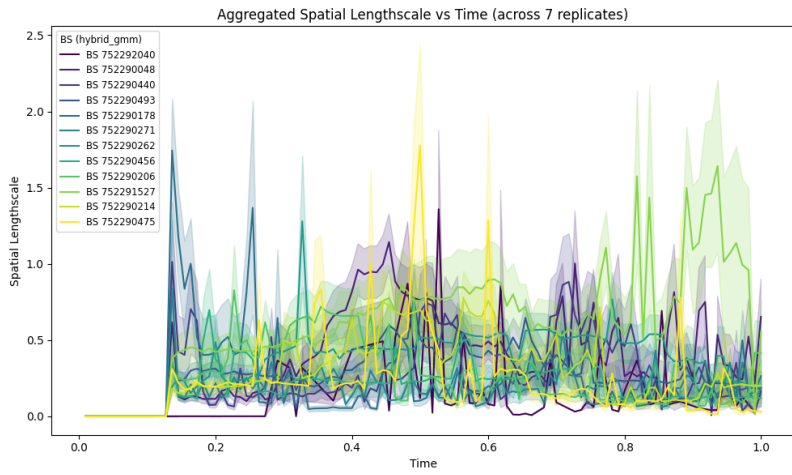


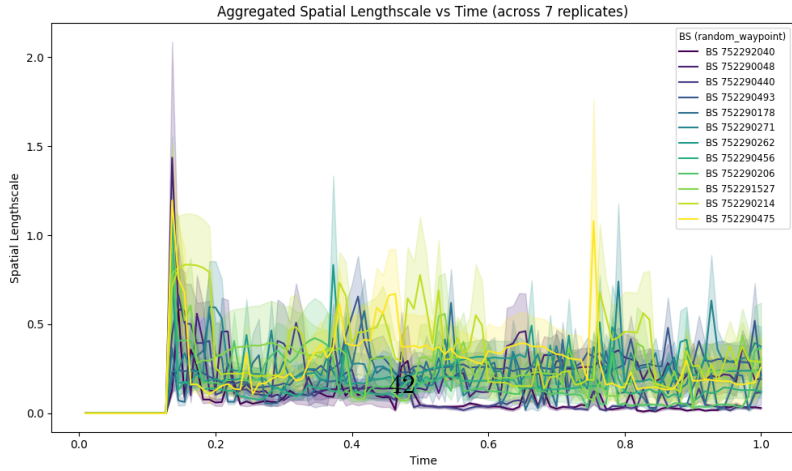
Figure 13: Spatial lengthscale vs. time across different mobility models. Aggregation of 7 replicates. Each subfigure shows the spatial lengthscale variation over time for a specific mobility model.



(a) Biased random walk.



(b) Hybrid-GMM.



(c) Random waypoint.